

AD-A260 725



2

RL-TR-91-139
In-House Report
April 1991

DTIC
ELECTE
MAR 1 1993
S C D



DUAL-SURFACE MAGNETIC-FIELD INTEGRAL EQUATION SOLUTION FOR BODIES OF REVOLUTION

James L. Schmitz

APPROVED FOR PUBLIC RELEASE; DISTRIBUTION UNLIMITED.

93-04175



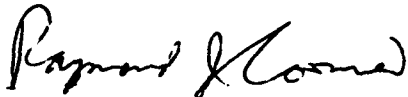
Rome Laboratory
Air Force Systems Command
Griffiss Air Force Base, NY 13441-5700

93 2 26 007

This report has been reviewed by the Rome Laboratory Public Affairs Division (PA) and is releasable to the National Technical Information Service (NTIS). At NTIS it will be releasable to the general public, including foreign nations.

RL-TR-91-139 has been reviewed and is approved for publication.

APPROVED:



RAYMOND J. CORMIER
Acting Chief, Applied Electromagnetics Division
Directorate of Electromagnetics

APPROVED:



JOHN K. SCHINDLER
Director of Electromagnetics

FOR THE COMMANDER:



JAMES W. HYDE III
Directorate of Plans & Programs

If your address has changed or if you wish to be removed from the Rome Laboratory mailing list, or if the addressee is no longer employed by your organization, please notify Rome Laboratory (EECT) Hanscom AFB MA 01731-5000. This will assist us in maintaining a current mailing list.

Do not return copies of this report unless contractual obligations or notices on a specific document require that it be returned.

REPORT DOCUMENTATION PAGE

Form Approved
OMB No. 0704-0188

Public reporting for this collection of information is estimated to average 1 hour per response, including the time for reviewing instructions, searching existing data sources, gathering and maintaining the data needed, and completing and reviewing the collection of information. Send comments regarding this burden estimate or any other aspect of this collection of information, including suggestions for reducing this burden, to Washington Headquarters Services, Directorate for Information Operations and Reports, 1215 Jefferson Davis Highway, Suite 1204, Arlington, VA 22202-4302, and to the Office of Management and Budget, Paperwork Reduction Project (0704-0188); Washington, DC 20503.

1. AGENCY USE ONLY (Leave blank)	2. REPORT DATE April 1991	3. REPORT TYPE AND DATES COVERED In-House May 88 to Dec 90	
4. TITLE AND SUBTITLE Dual-Surface Magnetic-Field Integral Equation Solution for Bodies of Revolution		5. FUNDING NUMBERS PE 61102F PR 2305 TA J4 WU 04	
6. AUTHOR(S) James L. Schmitz		8. PERFORMING ORGANIZATION REPORT NUMBER RL-TR-91-139	
7. PERFORMING ORGANIZATION NAME(S) AND ADDRESS(ES) Rome Laboratory (ERCT) Hanscom AFB, MA 01731-5000		10. SPONSORING/MONITORING AGENCY REPORT NUMBER	
9. SPONSORING/MONITORING AGENCY NAME(S) AND ADDRESS(ES)		10. SPONSORING/MONITORING AGENCY REPORT NUMBER	
11. SUPPLEMENTARY NOTES			
12a. DISTRIBUTION/AVAILABILITY STATEMENT Approved for public release; distribution unlimited		12b. DISTRIBUTION CODE	
13. ABSTRACT (Maximum 200 words) <p>Conventional magnetic-field integral equations for perfectly conducting bodies introduce spurious resonances at the resonant frequencies of the interior cavity formed by the scattering surface, yielding unreliable results for bodies larger than about a wavelength across. The spurious resonances can be eliminated from the magnetic-field integral equation by using the dual-surface magnetic-field integral equation derived by Yaghjian. The dual-surface magnetic-field integral equation, although identical in form and comparable in complexity to the original magnetic-field integral equation, provides a unique solution for the surface current \vec{J} at all frequencies. A computer program that computes the electromagnetic scattering from bodies of revolution using the dual-surface magnetic-field integral equation has been developed. The numerical results obtained from the body of revolution program using the dual-surface magnetic-field integral equation for a sphere, two frustums, and a truncated circular cylinder are compared to those of the exact Mie solution, a wire-mesh computer code, and measurements, respectively.</p>			
14. SUBJECT TERMS Scattering Radar cross section Surface integral equations		15. NUMBER OF PAGES 66	
17. SECURITY CLASSIFICATION OF REPORT Unclassified		16. PRICE CODE	
18. SECURITY CLASSIFICATION OF THIS PAGE Unclassified		20. LIMITATION OF ABSTRACT SAR	
19. SECURITY CLASSIFICATION OF ABSTRACT Unclassified		20. LIMITATION OF ABSTRACT SAR	

Accession For	
NTIS CRA&I	<input checked="" type="checkbox"/>
DTIC TAB	<input type="checkbox"/>
Unannounced	<input type="checkbox"/>
Justification _____	
By _____	
Distribution / _____	
Availability Codes	
Dist	Avail and/or Special
A-1	

Contents

1. INTRODUCTION	1
2. STATEMENT OF PROBLEM	3
3. MAGNETIC-FIELD INTEGRAL EQUATION	5
3.1 Formulation	5
3.2 Far-Field	15
3.3 Numerical Results	17
4. DUAL-SURFACE MAGNETIC-FIELD INTEGRAL EQUATION	18
4.1 Formulation	18
4.2 Numerical Results	24
5. CONCLUSIONS	50
REFERENCES	53
APPENDIX	55

Illustrations

1. Body of Revolution and Coordinate System	4
2. Plane Wave Scattering by a Conducting Body of Revolution	4
3. Geometry of Perfect Conductor for Plane Wave Scattering	6
4. Geometry of Singularity Integration	8
5. Backscattering Cross Section Versus ka of a Perfectly Conducting Sphere Computed with the Original Magnetic-Field Integral Equation and the Mie Series	19
6. Geometry of Perfect Conductor for Dual-Surface Magnetic-Field Integral Equation	20
7. Backscattering Cross Section Versus ka of a Perfectly Conducting Sphere Computed with the Dual-Surface Magnetic-Field Integral Equation and the Mie Series .	25
8. Backscattering Cross Section Versus ka of a Perfectly Conducting Sphere Computed with the Dual-Surface Magnetic-Field Integral Equation, Combined-Field Integral Equation, and the Mie Series	27
9. Radar Cross Section Versus Bistatic Angle of a Perfectly Conducting Sphere Computed with the Dual-Surface Magnetic-Field Integral Equation and the Mie Series; $ka = 20$, $\theta_t = 0$, E-Plane	28
10. Radar Cross Section Versus Bistatic Angle of a Perfectly Conducting Sphere Computed with the Dual-Surface Magnetic-Field Integral Equation and the Mie Series; $ka = 20$, $\theta_t = 0$, H-Plane	29

11. Radar Cross Section Versus Bistatic Angle of a Perfectly Conducting Sphere Computed with the Dual-Surface Magnetic-Field Integral Equation and the Mie Series; $ka = 20$, $\theta_i = 90$, E-Plane	30
12. Radar Cross Section Versus Bistatic Angle of a Perfectly Conducting Sphere Computed with the Dual-Surface Magnetic-Field Integral Equation and the Mie Series; $ka = 20$, $\theta_i = 90$, H-Plane	31
13. Radar Cross Section Versus Bistatic Angle of a Perfectly Conducting Sphere Computed with the Dual-Surface Magnetic-Field Integral Equation and the Mie Series; $ka = 70$, $\theta_i = 0$, E-Plane	32
14. Radar Cross Section Versus Bistatic Angle of a Perfectly Conducting Sphere Computed with the Dual-Surface Magnetic-Field Integral Equation and the Mie Series; $ka = 70$, $\theta_i = 0$, H-Plane	33
15. Radar Cross Section Versus Bistatic Angle of a Perfectly Conducting Circular Cylinder Computed with the Dual-Surface Magnetic-Field Integral Equation and the OSU Code; $\theta_i = 0$, E-Plane	36
16. Radar Cross Section Versus Bistatic Angle of a Perfectly Conducting Circular Cylinder Computed with the Dual-Surface Magnetic-Field Integral Equation and the OSU Code; $\theta_i = 0$, H-Plane	37
17. Radar Cross Section Versus Bistatic Angle of a Perfectly Conducting Frustum Computed with the Dual-Surface Magnetic-Field Integral Equation and the OSU Code; $\theta_i = 0$, E-Plane	38
18. Radar Cross Section Versus Bistatic Angle of a Perfectly Conducting Frustum Computed with the Dual-Surface Magnetic-Field Integral Equation and the OSU Code; $\theta_i = 0$, H-Plane	39
19. Radar Cross Section Versus Bistatic Angle of a Perfectly Conducting Frustum Computed with the Dual-Surface Magnetic-Field Integral Equation and the OSU Code; $\theta_i = 180$, E-Plane	40
20. Radar Cross Section Versus Bistatic Angle of a Perfectly Conducting Frustum Computed with the Dual-Surface Magnetic-Field Integral Equation and the OSU Code; $\theta_i = 180$, H-Plane	41
21. Radar Cross Section Versus Bistatic Angle of a Perfectly Conducting Flat-Backed Cone Computed with the Dual-Surface Magnetic-Field Integral Equation and the OSU Code; $\theta_i = 0$, E-Plane	42
22. Radar Cross Section Versus Bistatic Angle of a Perfectly Conducting Flat-Backed Cone Computed with the Dual-Surface Magnetic-Field Integral Equation and the OSU Code; $\theta_i = 0$, H-Plane	43

23.	Radar Cross Section Versus Bistatic Angle of a Perfectly Conducting Flat-Backed Cone Computed with the Dual-Surface Magnetic-Field Integral Equation and the OSU Code; $\theta_t = 180$, E-Plane	44
24.	Radar Cross Section Versus Bistatic Angle of a Perfectly Conducting Flat-Backed Cone Computed with the Dual-Surface Magnetic-Field Integral Equation and the OSU Code; $\theta_t = 180$, H-Plane	45
25.	Backscattering Cross Section Versus ka of a Perfectly Conducting Circular Cylinder as Computed with the OSU Code; E-Plane	46
26.	Radar Cross Section Versus Bistatic Angle of a Perfectly Conducting Flat-Backed Cone Computed with the Dual-Surface Magnetic-Field Integral Equation (10.0 Segments Per Wavelength) and the OSU Code (10.0 and 11.8 Segments Per Wavelength); $\theta_t = 180$, E-Plane	47
27.	Backscattering Cross Section Versus Aspect Angle of a Perfectly Conducting Circular Cylinder as Computed with the Dual-Surface Magnetic-Field Integral Equation and Measurements; E-Plane	48
28.	Backscattering Cross Section Versus Aspect Angle of a Perfectly Conducting Circular Cylinder as Computed with the Dual-Surface Magnetic-Field Integral Equation and Measurements; H-Plane	49
A 1	Phi Integration Correction for Self-Patch	56

Acknowledgements

I am indebted to Dr. A. D. Yaghjian for his guidance and interest in this work, without which this report would never have been written.

Dual-Surface Magnetic-Field Integral Equation Solution for Bodies of Revolution

1. INTRODUCTION

Conventional solutions of the magnetic-field integral equation fail to produce a unique solution at frequencies equal to the resonant frequencies of the interior cavity.^{1,2} These spurious resonances severely corrupt the numerical solution of the magnetic-field integral equation. Yaghjian³ proved that the original magnetic-field integral equation allows spurious resonances at these frequencies because it does not restrict the tangential electric field to zero on the surface of the scatterer. Tobin, et al.⁴ derived the dual-surface magnetic-field integral

Received for Publication 1 May 1991

¹Murray, F.H. (1931) Conductors in an electromagnetic field, *Am. J. Math.*, 53:275-288.

²Maue, A.W. (1949) On the formulation of a general scattering problem by means of an integral equation, *Zeitschrift fur Physik*, 126(7/9):601-618.

³Yaghjian, A.D. (1981) Augmented electric and magnetic field integral equation, *Radio Science*, 16:987-1001.

⁴Tobin, A.R., Yaghjian, A.D., and Bell, M.M. (1987) Surface integral equations for multi-wavelength, arbitrarily shaped, perfectly conducting bodies, *Digest of the National Radio Science Meeting*, (URSI), Boulder, CO.

equation and applied it to a three-dimensional, multi-wavelength, perfectly conducting body. This numerical solution showed that the dual-surface magnetic-field integral equation did indeed eliminate the spurious resonances associated with the interior cavity modes. The solution of the dual-surface magnetic-field integral equation first appeared in Tobin, et al.⁴, and the proof of uniqueness and derivation for both the dual-surface electric-field integral equation and magnetic-field integral equation will appear⁵ in March, 1991.

Mautz and Harrington derived the combined-field integral equation solution⁶ to eliminate the spurious resonances associated with the interior cavity modes. The combined-field integral equation, as the name implies, combines the solution of the magnetic-field integral equation with the electric-field integral equation. The combined-field integral equation's main drawback is that it involves the solution of both the magnetic-field integral equation and the electric-field integral equation, therefore, additional programing ability and computer run-time are required compared with the original magnetic-field integral equation.

One application of the combined-field integral equation and dual-surface magnetic-field integral equation solutions is plane wave scattering from a body of revolution. As an alternative to the combined-field integral equation, a body of revolution solution was formulated using the dual-surface magnetic-field integral equation to determine if it was advantageous to use because of increased accuracy or decreased computer run-time. The body of revolution formulation of the dual-surface magnetic-field integral equation solution parallels the body of revolution formulation in Mautz et al.⁶ However, the numerical solution to the body of revolution dual-surface magnetic-field integral equation uses a single pulse and impulse approximation for basis and testing functions instead of the triangular basis and testing functions used in Mautz et al.⁶ The combined-field integral equation solution requires a more complicated set of basis and testing functions due to the inclusion of the electric-field integral equation. The different basis and testing functions are necessary to accurately model the derivative of the surface current in the electric-field integral equation. This derivative is not present in the magnetic-field integral equation. Also, summations for the integration use a simple rectangular rule rather than the more complex Gaussian quadrature integration scheme.

⁵Woodworth, M.B., and Yaghjian, A.D. (1989) Derivation, application and conjugate gradient solution of the dual-surface integral equations for three-dimensional, multi-wavelength perfect conductors, *PIERS-5: Applications of the Conjugate Gradient Method to Electromagnetic and Signal Analysis*, Sarkar, T.K. and Kong, J.A., eds., Elsevier; also RADC TR-89-142, Hanscom AFB, MA, ADA229076.

⁶Mautz, J.R., and Harrington, R.F. (1987) H-field, and combined-field solutions for bodies of revolution, *Arch. Electron. Ubertragungstech. (Electron. Commun.)*, **32(4)**:157-164.

Results from the dual-surface magnetic-field integral equation and combined-field integral equation body of revolution solutions are compared using a perfectly conducting sphere. The accuracy of the solutions and computer run-times are also compared to investigate the benefits and pitfalls of both solutions. Far-field results for the truncated and flat-back cones, as well as the truncated circular cylinder, are compared with the results of a wire-mesh computer code obtained from Ohio State University.⁷ The predicted radar cross section of the truncated circular cylinder is also compared with measured data over a wide range of aspect angles.

2. STATEMENT OF PROBLEM

It is desired to determine the scattered far field from a perfectly conducting body of revolution excited by a plane wave. Figure 1 shows the geometry and the coordinate system used for the body of revolution, where ρ , ϕ , and z are the cylindrical coordinates and t and ϕ form an orthogonal curvilinear coordinate system on the body of revolution surface S . \hat{u}_t and \hat{u}_ϕ are orthogonal unit vectors in the t and ϕ directions, respectively. Figure 2 shows the coordinate system for plane wave scattering. The propagation vector for the incident plane wave is \vec{k}_i , θ_i defines the the transmit angle, θ_r and ϕ_r are the receiver spherical angles defining the direction along which the scattered far field is observed, and \vec{k}_r is the receiver propagation vector, which points from the receiver location to the origin. Note that \vec{k}_i is limited to the xz -plane ($\phi_i = 0$). Figure 2 shows that \hat{u}_θ^i , \hat{u}_ϕ^i , \hat{u}_θ^r , and \hat{u}_ϕ^r are unit vectors in the θ_i , y , θ_r , and ϕ_r directions respectively. The notation follows basically that of Mautz and Harrington.⁶

⁷Wang, C.W. (1983) *Scattering From Rotationally Symmetric Conducting Body*, Ohio State University Electroscience Laboratory Tech. Rep. 714614-2, Columbus, Ohio.

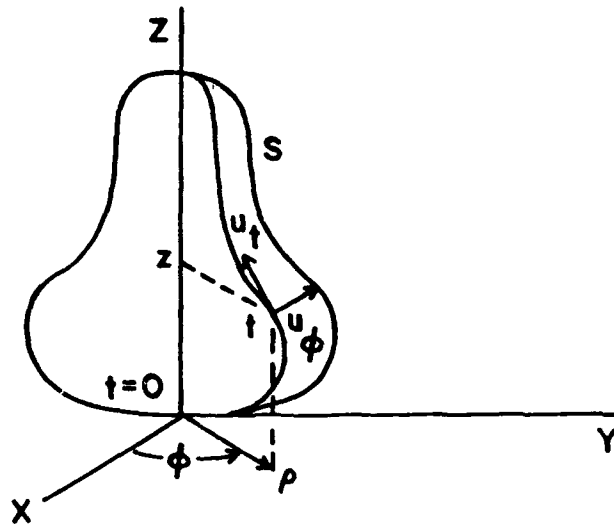


Figure 1. Body of Revolution and Coordinate System

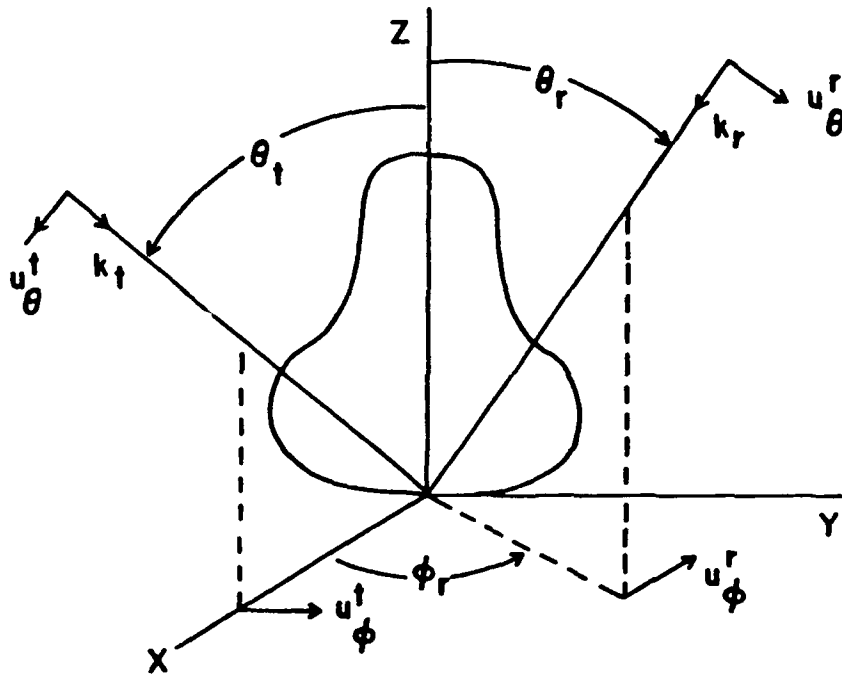


Figure 2. Plane Wave Scattering by a Conducting Body of Revolution

Considered separately is an incident plane wave (H^ϕ) defined by

$$\dot{H}_{inc} = (\dot{k}_t \times \dot{u}_\phi^t) e^{-jk_t r} \quad (1)$$

and an incident plane wave (H^θ) defined by

$$\dot{H}_{inc} = (\dot{k}_t \times \dot{u}_\phi^t) e^{-jk_t r}, \quad (2)$$

where \dot{H}_{inc} is the incident magnetic field, r is the position vector from the origin, k is the free space wavenumber, and η is the free space intrinsic impedance (using $e^{j\omega t}$ time dependence). The incident plane wave gives rise to electric currents directed in both the ϕ and t directions on the surface S as well as scattered far fields in the θ_r and ϕ_r directions.

3. MAGNETIC-FIELD INTEGRAL EQUATION

3.1 Formulation

Figure 3 illustrates an arbitrarily shaped body with a plane wave incident on the body. By definition of the scattered electric and magnetic fields,

$$\dot{E}(r') = \dot{E}_{sc} + \dot{E}_{inc} \quad (3)$$

and

$$\dot{H}(r') = \dot{H}_{sc} + \dot{H}_{inc}. \quad (4)$$

For the position vector r' not on the surface S

$$\dot{H}_{sc}(r') = \frac{1}{\mu_0} \nabla \times \dot{A}_{sc}(r'), \quad (5)$$

where

$$\dot{A}_{sc}(r') = \frac{\mu_0}{4\pi} \int_S \frac{\dot{J}(r'')}{|r' - r''|} e^{-jk|r' - r''|} dS''. \quad (6)$$

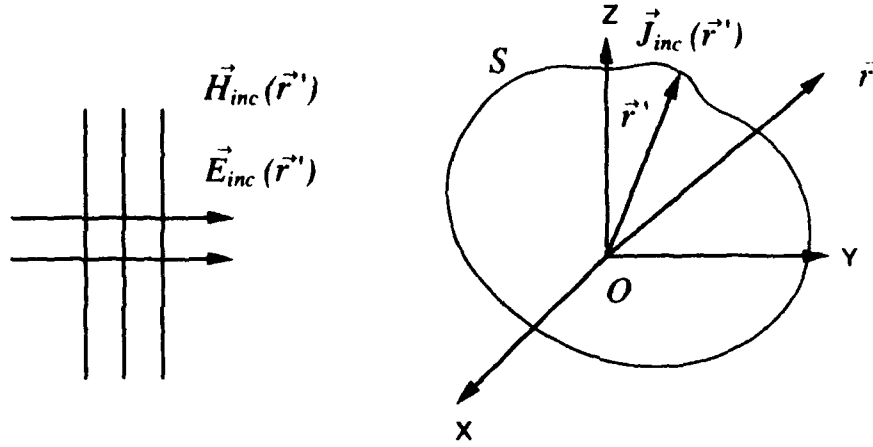


Figure 3. Geometry of Perfect Conductor for Plane Wave Scattering

Substituting for $\vec{A}_{sc}(\vec{r})$ in Eq. (5), the scattered magnetic field becomes

$$\vec{H}_{sc}(\vec{r}) = \frac{1}{4\pi} \int_S \vec{J}(\vec{r}') \times \nabla' \psi dS', \quad (7)$$

where

$$\psi = \frac{e^{-jk|\vec{r}-\vec{r}'|}}{|\vec{r}-\vec{r}'|}. \quad (8)$$

For \vec{r} inside the sphere, $\vec{E}(\vec{r})$ and $\vec{H}(\vec{r})$ equal zero from the boundary conditions at the surface, and thus

$$\vec{H}_{sc}(\vec{r}) = -\vec{H}_{inc}(\vec{r}). \quad (9)$$

Substituting $\vec{H}_{sc}(\vec{r})$ from Eq. (9) into Eq. (7) we obtain

$$-\vec{H}_{inc}(\vec{r}) = \frac{1}{4\pi} \int_S \vec{J}(\vec{r}') \times \nabla' \psi dS' \quad (\vec{r} \text{ inside } S). \quad (10)$$

As \vec{r} approaches S from inside the surface,

$$\int_S \vec{J}(\vec{r}') \times \nabla' \psi dS' = \oint_S \vec{J}(\vec{r}') \times \nabla' \psi dS' + \int_S \vec{J}(\vec{r}') \times \nabla' \psi dS', \quad (11)$$

where \oint denotes the principal-value surface integral evaluated by excluding the singular point with a circular "principal area" ³ and \oint is the integration over the small circular patch as \vec{r} approaches S , i.e. as $\epsilon/\delta \rightarrow 0$ in Figure 4. At \vec{r} near \vec{r}' , $\vec{J}(\vec{r}) \approx \vec{J}(\vec{r}')$. Therefore,

$$\oint \vec{J}(\vec{r}') \times \nabla' \psi dS' = \vec{J}(\vec{r}) \times \oint \nabla' \psi dS'. \quad (12)$$

Figure 4 shows that for the small patch where $\vec{r} \rightarrow \vec{r}'$

$$|\vec{r} - \vec{r}'| = \rho'^2 + \epsilon^2 \equiv R'^2, \quad (13)$$

and therefore

$$\oint \nabla' \psi dS' = \oint \nabla' \left(\frac{1}{R'} \right) \rho' d\phi' d\rho' \quad (14)$$

where

$$\nabla' \left(\frac{1}{R'} \right) = -\frac{\hat{R}'}{R'^2}, \quad (15)$$

and

$$\hat{R}' = R'_\rho \hat{\rho}' + R'_\phi \hat{\phi}' + R'_z \hat{z}'. \quad (16)$$

Substituting for ϵ ,

$$\hat{R}' = \frac{\rho'}{R'} \hat{\rho}' + \frac{\epsilon}{R'} \hat{z}'. \quad (17)$$

Evaluating Eq. (14) with Eq. (17) leads to

$$\oint \nabla' \psi dS' = -2\pi \hat{n}, \quad (18)$$

and therefore

$$\vec{J}(\vec{r}) \times \oint \nabla' \psi dS' = -\vec{J}(\vec{r}) \times 2\pi \hat{n}. \quad (19)$$

Making these substitutions in Eq. (10) and taking \hat{n} cross both sides we obtain the magnetic-field integral equation

$$-\hat{n} \times \vec{H}_{inc}(\vec{r}) = \hat{n} \times \frac{1}{4\pi} \oint_S \vec{J}(\vec{r}') \times \nabla' \psi dS' - \frac{\vec{J}(\vec{r})}{2}. \quad (20)$$

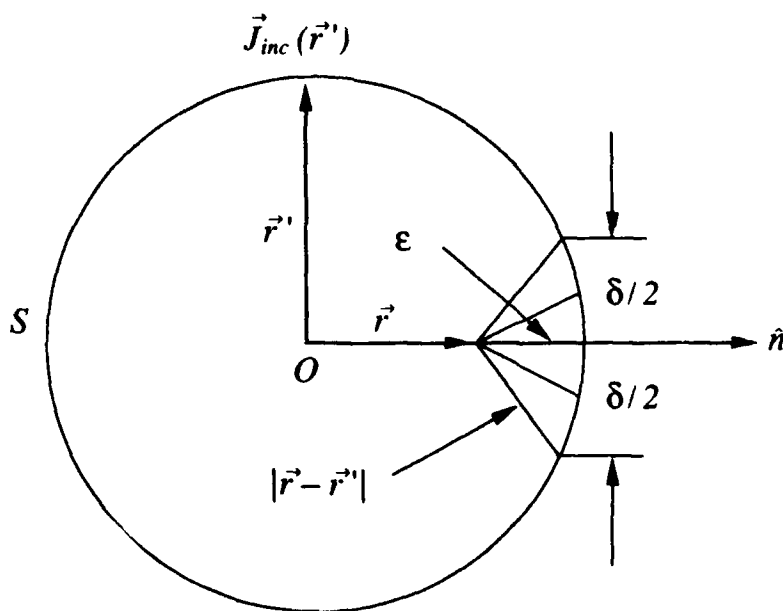


Figure 4. Geometry of Singularity Integration

This derivation was for a circular "principal area", but Yaghjian³ shows that this derivation holds for any shaped "principal area" excluding the singularity in the integrand of Eq. (20). Using the vector relationship

$$\vec{J}(\vec{r}') \times \nabla' \psi = - \left(\frac{1 + jk|\vec{r} - \vec{r}'|}{|\vec{r} - \vec{r}'|^3} \right) e^{-jk|\vec{r} - \vec{r}'|} (\vec{r} - \vec{r}') \times \vec{J}(\vec{r}'), \quad (21)$$

Eq. (20) becomes

$$\hat{n} \times \vec{H}_{inc}(\vec{r}) = \frac{\vec{J}(\vec{r})}{2} + \frac{1}{4\pi} \oint_S \left(\frac{1 + jk|\vec{r} - \vec{r}'|}{|\vec{r} - \vec{r}'|^3} \right) e^{-jk|\vec{r} - \vec{r}'|} \hat{n} \times [(\vec{r} - \vec{r}') \times \vec{J}(\vec{r}')] dS' \quad (22)$$

for \vec{r} on S . The outward normal \hat{n} is defined as $\hat{n} = \hat{u}_\phi \times \hat{u}_t$. Using the notation in Reference 6 and letting

$$\vec{J}(\vec{r}') = \hat{u}'_t J^t(t', \phi') + \hat{u}'_\phi J^\phi(t', \phi'), \quad (23)$$

where \hat{u}'_t and \hat{u}'_ϕ are unit vectors in the t' and ϕ' directions respectively, Eq. (22) expands to

$$\begin{aligned} \hat{u}_t \left\{ \frac{J^t(t, \phi)}{2} + \frac{k^3}{4\pi} \int \rho' dt' \int_0^{2\pi} d\phi' G J^t(t', \phi' + \phi) [((\rho' - \rho) \cos v' \right. \\ \left. - (z' - z) \sin v') \cos \phi' - 2\rho \cos v' \sin^2(\frac{\phi'}{2})] \right. \\ \left. + \frac{k^3}{4\pi} \int \rho' dt' \int_0^{2\pi} d\phi' G J^\phi(t', \phi' + \phi) (z' - z) \sin \phi' \right\} \\ + \hat{u}_\phi \left\{ \frac{J^\phi(t, \phi)}{2} + \frac{k^3}{4\pi} \rho' dt' \int_0^{2\pi} d\phi' G J^t(t', \phi' + \phi) (\rho' \sin v \cos v' \right. \\ \left. - \rho \sin v' \cos v - (z' - z) \sin v \sin v') \sin \phi' \right. \\ \left. + \frac{k^3}{4\pi} \int \phi' dt' \int_0^{2\pi} d\phi' G J^\phi(t', \phi' + \phi) [((\rho' - \rho) \cos v \right. \\ \left. - (z' - z) \sin v) \cos \phi' + 2\rho' \cos v \sin^2(\frac{\phi'}{2})] \right\} = \hat{n} \times \vec{H}_{inc}, \quad (24) \end{aligned}$$

where

$$G = \frac{1 + jkR}{k^3 R^3} e^{-jkR} \quad (25)$$

and

$$R = \sqrt{(\rho - \rho')^2 + (z - z')^2 + 4\rho\rho' \sin^2(\frac{\phi'}{2})}. \quad (26)$$

In Eq. (24), both \hat{n} and \vec{k}_t are to be evaluated on S at t and ϕ . The angle v between \hat{u}_t and the z -axis is positive when \hat{u}_t points away from the z -axis and is negative when \hat{u}_t points toward the z -axis. The primed variables are functions of t' and therefore are evaluated at t' .

We want to take advantage of the geometry of the body of revolution by separating the ϕ and t dependence of \vec{J}_t and \vec{J}_ϕ . To accomplish this, \vec{J}_t and \vec{J}_ϕ are expanded in a Fourier series in ϕ :

$$J^t(t, \phi) = \sum_{n=-\infty}^{\infty} j_n^t(t) e^{jn\phi} \quad (27)$$

$$J^\phi(t, \phi) = \sum_{n=-\infty}^{\infty} j_n^\phi(t) e^{jn\phi} \quad (28)$$

$$J^t(t', \phi' + \phi) = \sum_{n=-\infty}^{\infty} j_n^t(t') e^{jn(\phi' + \phi)} \quad (29)$$

$$J^\phi(t', \phi' + \phi) = \sum_{n=-\infty}^{\infty} j_n^\phi(t') e^{jn(\phi' + \phi)}. \quad (30)$$

The \hat{u}_t and \hat{u}_ϕ components of Eq. (24) will be evaluated given an H^ϕ polarized incident wave. For the \hat{u}_t component, substituting for $J^t(t, \phi)$, $J^\phi(t, \phi)$, $J^t(t', \phi' + \phi)$, and $J^\phi(t', \phi' + \phi)$ in Eq. (24) yields

$$\begin{aligned} \sum_{n=-\infty}^{\infty} j_n^t(t) e^{jn\phi} + K_1(t', \phi') \sum_{n=-\infty}^{\infty} j_n^t(t') e^{jn(\phi' + \phi)} \\ + K_2(t', \phi') \sum_{n=-\infty}^{\infty} j_n^\phi(t') e^{jn(\phi' + \phi)} = -k \cos \phi e^{j\vec{k}_i \cdot \vec{r}} \end{aligned} \quad (31)$$

where $K_1(t, t', \phi')$ and $K_2(t, t', \phi')$ are the known portions of Eq. (24) that depend on t, t' , and ϕ' . The functions of t' , $j_n^t(t')$ and $j_n^\phi(t')$, are the unknown Fourier coefficients. The expression on the right side of Eq. (31) is the \hat{u}_t component of $\hat{n} \times \vec{H}_{inc}$ for the H^ϕ polarized incident wave.

Since we have an $e^{jn\phi}$ in each term on the left side of Eq. (31), we will multiply both sides by $e^{-jm\phi}$ and integrate both sides from $-\pi$ to π with respect to ϕ . The integral on the left side of Eq. (31) is zero if $m \neq n$ and π if $m = n$ (applying orthogonality). Evaluating the right side of Eq. (24) for the \hat{u}_ϕ component of the H^ϕ polarized incident wave where

$$\vec{k}_i \cdot \vec{r} = -k(\rho \cos \phi \sin \theta_i + z \cos \theta_i), \quad (32)$$

we have

$$\int_0^{2\pi} [-k \cos \phi e^{jk(\rho \cos \phi \sin \theta_i + z \cos \theta_i)} e^{-jm\phi}] d\phi. \quad (33)$$

We can evaluate this integral using Bessel functions with

$$J_m(r) = \frac{1}{2\pi} j^m \int_0^{2\pi} e^{jr \cos \phi - jm\phi} d\phi$$

for $m = 0, \pm 1, \pm 2, \dots$ (34)

The right side of Eq. (31) using Eq. (34) equals

$$-\pi k e^{jkz \cos \theta_t} j^{n+1} [J_{n+1}(k\rho \sin \theta_t) - J_{n-1}(k\rho \sin \theta_t)]. \quad (35)$$

We go through the same substitution as for the \hat{u}_t component of the H^ϕ polarized incident wave for $J^t(t, \phi)$, $J^\phi(t, \phi)$, $J^t(t', \phi' + \phi)$, and $J^\phi(t', \phi' + \phi)$ in Eq. (24). The integral on the right side of Eq. (24) is

$$\int_0^{2\pi} [k \sin \phi \sin t e^{jkz \cos \phi \sin \theta_t + z \cos \theta_t} e^{-jm\phi}] d\phi. \quad (36)$$

Using Eq. (34) reduces this integral to

$$\pi k \sin t e^{jkz \cos \theta_t} j^n [J_{n-1}(k\rho \sin \theta_t) + J_{n+1}(k\rho \sin \theta_t)]. \quad (37)$$

When we use the same approach for the H^θ polarized incident wave, the \hat{u}_t component is

$$\pi k \cos \theta_t e^{jkz \cos \theta_t} j^n [J_{n-1}(k\rho \sin \theta_t) + J_{n+1}(k\rho \sin \theta_t)], \quad (38)$$

and the \hat{u}_ϕ component is

$$k e^{jkz \cos \theta_t} [2\pi \cos t \sin \theta_t j J_n(k\rho \sin \theta_t) - \sin t \cos \theta_t \pi j^{n+1} (J_{n+1}(k\rho \sin \theta_t) - J_{n-1}(k\rho \sin \theta_t))]. \quad (39)$$

Rewriting Eq. (24), we find that the \hat{u}_t component of the H^ϕ incident wave is

$$\begin{aligned} \frac{J_n^t(t)}{2} + \frac{k^3}{4\pi} \int \rho' dt' j_n^t(t') \int_0^{2\pi} d\phi' e^{jm\phi'} G[(\rho' - \rho) \cos v' \\ - (z' - z) \sin v'] \cos \phi' - 2\rho \cos v' \sin^2(\frac{\phi'}{2})] \\ + \frac{k^3}{4\pi} \int \rho' dt' j_n^\phi(t') \int_0^{2\pi} d\phi' e^{jm\phi'} G[(z' - z) \sin \phi' \\ - \frac{k}{2} e^{jkz \cos \theta_t} j^{n+1} [J_{n+1}(k\rho \sin \theta_t) - J_{n-1}(k\rho \sin \theta_t)]]. \end{aligned} \quad (40)$$

and the \hat{u}_ϕ component of the H^ϕ incident wave is

$$\begin{aligned}
& \frac{j_n^\phi}{2} + \frac{k^3}{4\pi} \rho' dt' j_n^i(t') \int_0^{2\pi} d\phi' e^{jn\phi'} G(\phi' \sin v \cos v' \\
& \quad - \rho \sin v' \cos v - (z' - z) \sin v \sin v') \sin \phi' \\
& \quad + \frac{k^3}{4\pi} \int \phi' dt' j_n^\phi(t') \int_0^{2\pi} d\phi' e^{jn\phi'} G[(\rho' - \rho) \cos v \\
& \quad - (z' - z) \sin v) \cos \phi' + 2\rho' \cos v \sin^2(\frac{\phi'}{2})] \\
& = \frac{k}{2} \sin v e^{jkz \cos \theta_i} [j^{n-2} J_{n+1}(k\rho \sin \theta_i) - j^n J_{n-1}(k\rho \sin \theta_i)]. \tag{41}
\end{aligned}$$

For the H^θ incident plane wave, the \hat{u}_t component is

$$\begin{aligned}
& \frac{j_n^t(t)}{2} + \frac{k^3}{4\pi} \int \rho' dt' j_n^i(t') \int_0^{2\pi} d\phi' e^{jn\phi'} G[(\rho' - \rho) \cos v' \\
& \quad - (z' - z) \sin v') \cos \phi' - 2\rho \cos v' \sin^2(\frac{\phi'}{2})] \\
& \quad + \frac{k^3}{4\pi} \int \rho' dt' j_n^\phi(t') \int_0^{2\pi} d\phi' e^{jn\phi'} G(z' - z) \sin \phi' \\
& = -\frac{k}{2} \cos \theta_i e^{jkz \cos \theta_i} j^n [J_{n+1}(k\rho \sin \theta_i) + J_{n-1}(k\rho \sin \theta_i)], \tag{42}
\end{aligned}$$

and the \hat{u}_ϕ component,

$$\begin{aligned}
& \frac{j_n^\phi(t)}{2} + \frac{k^3}{4\pi} \rho' dt' j_n^i(t') \int_0^{2\pi} d\phi' e^{jn\phi'} G(\phi' \sin v \cos v' \\
& \quad - \rho \sin v' \cos v - (z' - z) \sin v \sin v') \sin \phi' \\
& \quad + \frac{k^3}{4\pi} \int \phi' dt' j_n^\phi(t') \int_0^{2\pi} d\phi' e^{jn\phi'} G[(\rho' - \rho) \cos v \\
& \quad - (z' - z) \sin v) \cos \phi' + 2\rho' \cos v \sin^2(\frac{\phi'}{2})]
\end{aligned}$$

$$\begin{aligned}
&= ke^{jkz \cos \theta_i} [2\pi \cos v \sin \theta_i j J_n(k\rho \sin \theta_i) \\
&\quad - \sin v \cos \theta_i \pi j^{m+1} (J_{n+1}(k\rho \sin \theta_i) - J_{n+1}(k\rho \sin \theta_i))]. \tag{43}
\end{aligned}$$

The t , t' and ϕ' integrations can be converted to direct summations. Dividing the t and t' integrals into discrete segments, we evaluate the integrand at the center of each segment and then sum over the number of t - and t' -segments. The ϕ' integral is divided into small patches, again approximating the integrand at the center of each patch. In moment method terminology, this equates to using pulse basis functions and unit impulse testing functions. The well-behaved condition of the magnetic-field integral equation allows such simple basis and testing functions to be used.

Rewriting Eqs. (40) and (41) with the t' and ϕ' integrations represented as summations, we have

$$\begin{aligned}
\frac{j_{nl}^t}{2} + \Delta t \sum_{\substack{m=1 \\ m \neq l}}^M K_n^{tt}(t_l, t_m) j_{nm}^t + \Delta t \sum_{\substack{m=1 \\ m \neq l}}^M K_n^{t\phi}(t_l, t_m) j_{nm}^\phi = S_n^t(t_l, \theta_i) \\
\text{for } l = 1, 2, \dots, M, \tag{44}
\end{aligned}$$

and

$$\begin{aligned}
\frac{j_{nl}^\phi}{2} + \Delta t \sum_{\substack{m=1 \\ m \neq l}}^M K_n^{\phi t}(t_l, t_m) j_{nm}^t + \Delta t \sum_{\substack{m=1 \\ m \neq l}}^M K_n^{\phi\phi}(t_l, t_m) j_{nm}^\phi = S_n^\phi(t_l, \theta_i) \\
\text{for } l = 1, 2, \dots, M, \tag{45}
\end{aligned}$$

where n is the mode number, l is the number of the t -segment, and m the segment number for the t' integration. The first superscript indicates the direction of the current and the second superscript indicates the vector component. M is the maximum number of t - and t' -segments, and Δt is the length of the t -segment.

For a given $t(l)$ and $t'(m)$ the only unknown quantities in Eqs. (44) and (45) are j_n^t and j_n^ϕ . Thus for a given n , t , and t' , Eqs. (44) and (45) can be represented as

$$\begin{bmatrix} K_{11}^{tt} & \dots & K_{1M}^{tt} & K_{11}^{t\phi} & \dots & K_{1M}^{t\phi} \\ \vdots & \dots & \vdots & \vdots & \dots & \vdots \\ K_{M1}^{tt} & \dots & K_{MM}^{tt} & K_{M1}^{t\phi} & \dots & K_{MM}^{t\phi} \\ K_{11}^{\phi t} & \dots & K_{1M}^{\phi t} & K_{11}^{\phi\phi} & \dots & K_{1M}^{\phi\phi} \\ \vdots & \dots & \vdots & \vdots & \dots & \vdots \\ K_{M1}^{\phi t} & \dots & K_{MM}^{\phi t} & K_{M1}^{\phi\phi} & \dots & K_{MM}^{\phi\phi} \end{bmatrix} \begin{bmatrix} j_1^t \\ \vdots \\ j_M^t \\ j_1^\phi \\ \vdots \\ j_M^\phi \end{bmatrix} = \begin{bmatrix} S_1^t \\ \vdots \\ S_M^t \\ S_1^\phi \\ \vdots \\ S_M^\phi \end{bmatrix} \quad (46)$$

where K and S are known functions of t, t', ϕ , and t and θ_t , respectively and the j 's are the unknown Fourier series coefficients of the current.

The superscripts of the j and S variables indicate the vector component, and the subscripts indicate the segment. This square matrix equation can be solved for j_n^t and j_n^ϕ for each n , and the currents can be found from j_n^t and j_n^ϕ by using Eqs. (27) and (30).

Evaluating the ϕ' integration in Eqs. (40) and (43) at $t = t'$ ($\rho = \rho'$ and $z = z'$) yields $R = 2\rho \sin(\phi'/2)$. Therefore, at $t = t'$, the phi integration does not converge. This lack of convergence is not due to the magnetic-field integral equation but to our separation of the ϕ' and t' integrations. To obtain convergence at $t = t'$, one must evaluate the $\phi't'$ area integration more carefully. In Appendix A, it is shown that the ϕ' integration can be done properly, when the ϕ' integration is separated from the t' integration, if the modified Green's function

$$G = \frac{1}{k^3 R^2 R_c} + \frac{1}{k^3 R_c^3} [(1 + jkR_c)e^{-jkR_c} - 1] \quad (47)$$

replaces G in Eq. (25), where

$$R_c = \sqrt{(\Delta t/2)^2 + (\rho\phi')^2} \quad (48)$$

$$R_a = \sqrt{(\Delta t/2)^2/4 + (\rho\phi')^2} \quad (49)$$

and Δt is the size of the t -segment.

3.2 Far Field

To obtain the scattered magnetic far field, let $r \gg r'$ in Eq. (7) to get

$$\vec{H}_{sc}(\vec{r}) = -\frac{-jke^{jkr}}{4\pi r} \hat{r} \times \int_S \vec{J}(\vec{r}') e^{jk\hat{r} \cdot \vec{r}'} dS' \quad (50)$$

Noting that

$$\hat{r} \times \hat{u}_\phi = -\cos(\phi - \phi') \hat{u}_\theta + \cos\theta \sin(\phi - \phi') \hat{u}_\phi \quad (51)$$

$$\hat{r} \times \hat{u}_t = \sin(\phi - \phi') \sin v' \hat{u}_\theta + \cos\theta \cos(\phi - \phi') \sin v' \hat{u}_\phi \quad (52)$$

$$\hat{r}_r \cdot \vec{r}' = \rho' \sin\theta_r \cos(\phi - \phi') + z' \cos\theta \quad (53)$$

Eq. (50) can be written as

$$\begin{aligned} H_{sc}^\theta(\vec{r}) = & \frac{-jke^{jkr}}{4\pi r} \int_0^T \int_0^{2\pi} [J^\phi(\phi', t')(-\cos(\phi - \phi')) \\ & + J^t(\phi', t')(\sin(\phi - \phi') \sin v')] e^{jk(\rho' \sin\theta \cos(\phi - \phi') + z' \cos\theta)} d\phi' \rho' dt' \end{aligned} \quad (54)$$

and

$$\begin{aligned} H_{sc}^\phi(\vec{r}) = & \frac{-jke^{jkr}}{4\pi r} \int_0^T \int_0^{2\pi} [J^\phi(\phi', t')(-\sin(\phi - \phi') \cos\theta) \\ & + J^t(\phi', t')(-\sin\theta \cos v' + \cos(\phi - \phi') \cos\theta \sin v')] \\ & e^{jk(\rho' \sin\theta \cos(\phi - \phi') + z' \cos\theta)} d\phi' \rho' dt' \end{aligned} \quad (55)$$

where, according to Eqs. (27) and (28)

$$J^t(\phi', t') = \sum_{n=-\infty}^{\infty} j_n^t(t') e^{jn\phi'} \quad (56)$$

$$J^\phi(\phi', t') = \sum_{n=-\infty}^{\infty} j_n^\phi(t') e^{jn\phi'}. \quad (57)$$

The superscripts θ and ϕ designate the components of the scattered field. Substituting Eqs. (56) and (57) into Eq. (54) and using Eq. (34), Eq. (54) is rewritten as

$$H_{sc}^{\theta}(\vec{r}) = \frac{-jk e^{jkr}}{4\pi r} \int_0^T \sum_{n=-\infty}^{\infty} \left\{ j_n^{\phi}(t') e^{jn\phi} e^{jkz' \cos \theta} \pi j^{n+1} \right. \\ \left. [J_{n+1}(k\rho' \sin \theta) - J_{n-1}(k\rho' \sin \theta)] + j_n^t(t') e^{jn\phi} e^{jkz' \cos \theta} \pi \sin v' j^n \right. \\ \left. [J_{n+1}(k\rho' \sin \theta) + J_{n-1}(k\rho' \sin \theta)] \right\} \rho' dt' \quad (58)$$

and Eq. (55) as

$$H_{sc}^{\phi}(\vec{r}) = \frac{-jk e^{jkr}}{4\pi r} \int_0^T \sum_{n=-\infty}^{\infty} \left\{ j_n^{\phi}(t') e^{jn\phi} e^{jkz' \cos \theta} \pi \cos \theta j^n \right. \\ \left. [J_{n+1}(k\rho' \sin \theta) - J_{n-1}(k\rho' \sin \theta)] \right. \\ \left. + j_n^t(t') e^{jn\phi} e^{jkz' \cos \theta} \pi j^n [2 \sin \theta \cos v' J_n(k\rho' \sin \theta) - \cos \theta \sin v' j \right. \\ \left. (J_{n+1}(k\rho' \sin \theta) - J_{n-1}(k\rho' \sin \theta))] \right\} \rho' dt'. \quad (59)$$

The radar cross section σ is defined as

$$\sigma = \lim_{r \rightarrow \infty} 4\pi r^2 \frac{|\vec{H}_{sc}|^2}{|\vec{H}_{inc}|^2}. \quad (60)$$

For a \vec{H}_{θ} incident wave Eq. (60) becomes

$$\sigma = \lim_{r \rightarrow \infty} 4\pi r^2 \frac{|H_{sc}^{\theta\theta}|^2 + |H_{sc}^{\theta\phi}|^2}{|\vec{H}_{inc}|^2} \quad (61)$$

and for a \vec{H}_{ϕ} incident wave Eq. (60) becomes

$$\sigma = \lim_{r \rightarrow \infty} 4\pi r^2 \frac{|H_{sc}^{\phi\phi}|^2 + |H_{sc}^{\phi\theta}|^2}{|\vec{H}_{inc}|^2} \quad (62)$$

where the first and second superscripts designate the components of the incident and scattered fields, respectively.

For the plane wave incident along the positive z -axis, only the ± 1 modes are needed in the Fourier series to represent \vec{J}^i and \vec{J}^ϕ . For an incident plane wave off the z -axis, the number of modes n was chosen as

$$n = (1.1kr \sin \theta_i + 2) \quad (63)$$

where r is the maximum radius of the body of revolution measured from the z -axis.⁸ The reactive fields of the scatterer are extremely small for $n > kr$. Assuming the number of far-field fluctuations per solid angle are roughly the same in all directions, the far-field variations with ϕ will be less near the z -axis. Therefore, the number of modes needed to expand the field will become less as one approaches the z -axis, since the higher order modes which represent the more rapidly varying parts of the field, will not be needed to expand the slower variations with ϕ . This demonstrates that the maximum number of modes needed to represent the far field at the angle θ_i is approximately $ka \sin \theta_i$. The addition of the extra two modes was determined by the examination of results of the code for different number of modes.

Typically five to ten segments per wavelength are used for both the number of t -segments and ϕ -segments. The criterion for the number of ϕ -segments is based on having square patches for the ϕ integration. Other shaped patches were used, but the results proved most accurate for square or approximately square patches.

3.3 Numerical Results

Figure 5 is a plot of the normalized radar cross section $\sigma/\pi a^2$ in the backscattering direction from a sphere computed using the magnetic-field integral equation and the Mie series^{9,10} with the incident wave along the positive z -axis. The Mie series is an exact analytical solution for the scattering from spheres only and cannot be used to validate the dual-surface magnetic-field integral equation solution for other geometries.

⁸Yaghjian, A.D. (1977) *Near Field Antenna Measurements on A Cylindrical Surface: A Source Scattering-matrix Formulation*, NBS Technical Note 696.

⁹DiBeneditto, J.P. (1984) *Bistatic Scattering from Conducting Calibration Spheres*, RADC-TR-84-93, Hanscom AFB, MA, ADA154173.

¹⁰Stratton, J.A. (1941) *Electromagnetic Theory*, McGraw-Hill, New York.

Figure 5 shows that the magnetic-field integral equation solution contains spurious resonances at the interior cavity resonance frequencies of 2.744, 3.870, 4.973, 5.763, 6.062, 6.988, 7.140, 8.183, 8.211, 9.275, and 9.356.¹¹ The limitations of the magnetic-field integral equation are clearly demonstrated by Figure 5.

4. DUAL-SURFACE MAGNETIC-FIELD INTEGRAL EQUATION

4.1 Formulation

The following derivation and proof of uniqueness of the dual-surface magnetic-field integral equation closely follows the work on the dual-surface magnetic-field integral equation presented by Yaghjian.⁵ The dual-surface magnetic-field integral equation can be derived by beginning with Eq. (10), the "interior" or "extended" magnetic-field integral equation, which is rewritten here

$$-\vec{H}_{inc}(\vec{r}) = \frac{1}{4\pi} \int_S \vec{J}(\vec{r}') \times \nabla' \psi dS' \quad (\vec{r} \text{ inside } S). \quad (64)$$

The current $\vec{J}(\vec{r})$ in Eq. (64) is uniquely determined at every frequency if Eq. (64) is satisfied for all \vec{r} inside S .¹²

¹¹Harrington, R.F. (1961) *Time-Harmonic Electromagnetic Fields*, McGraw-Hill, New York.

¹²Waterman, P.C. (1965) Matrix formulation of electromagnetic scattering, *Proc. IEEE*, 53:805-812.

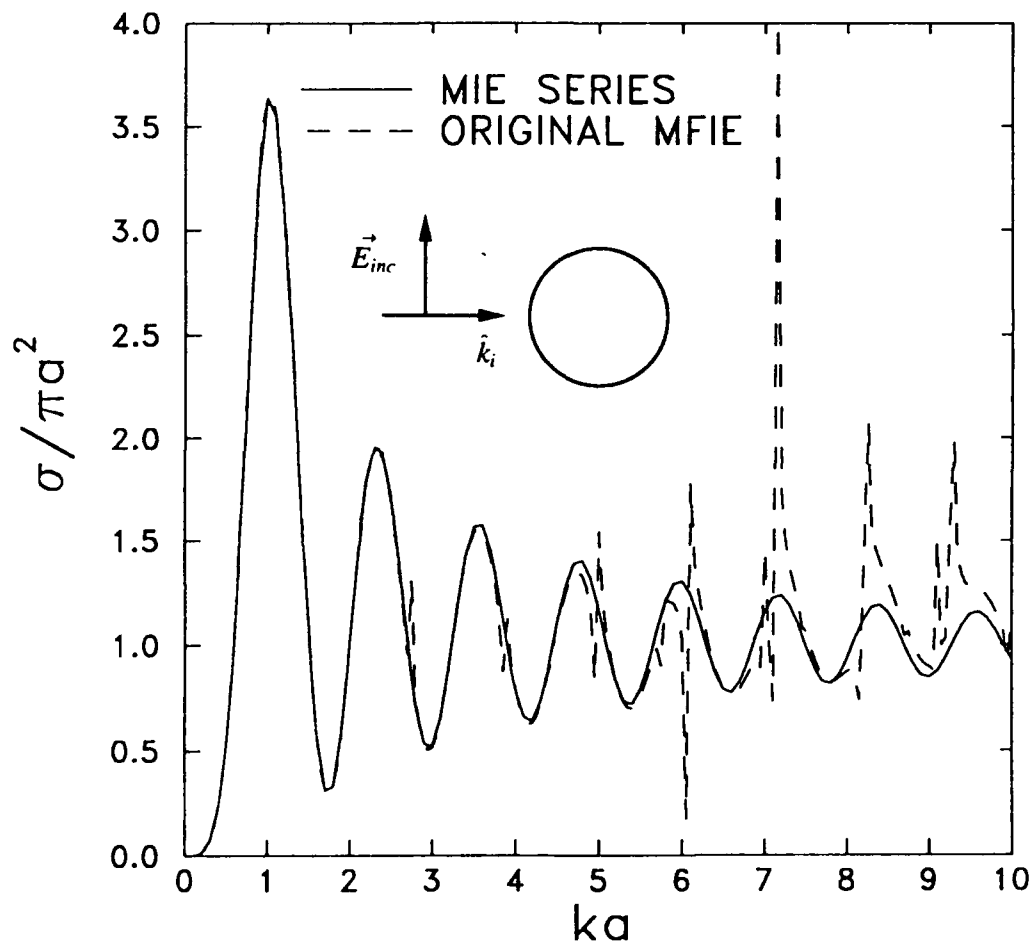


Figure 5. Backscattering Cross Section Versus ka of a Perfectly Conducting Sphere Computed with the Original Magnetic-Field Integral Equation and the Mie Series

Figure 6 shows the surface S and a surface S_δ parallel to, and some distance $\delta > 0$, inside of S .

By adding $\alpha \hat{n}$ cross Eq. (64) at points \vec{r} on S_δ to the corresponding points on S in the original magnetic-field integral equation, one obtains the dual-surface magnetic-field integral equation:⁵

$$\hat{n} \times \vec{H}_0(\vec{r}) = \frac{\vec{J}(\vec{r})}{2} - \hat{n} \times \frac{1}{4\pi} \oint_S \vec{J}(\vec{r}') \times \nabla' \psi_0(\vec{r}, \vec{r}') dS' \quad (65)$$

where

$$\vec{H}_0(\vec{r}) \equiv \vec{H}_{inc}(\vec{r}) + \alpha \vec{H}_{inc}(\vec{r} - \delta \hat{n}) \quad (66)$$

$$\psi_0(\vec{r}, \vec{r}') \equiv \psi(\vec{r}, \vec{r}') + \alpha \psi(\vec{r} - \delta \hat{n}, \vec{r}') \quad (67)$$

and, as usual

$$\psi = \frac{e^{-jk|\vec{r} - \vec{r}'|}}{|\vec{r} - \vec{r}'|}. \quad (68)$$

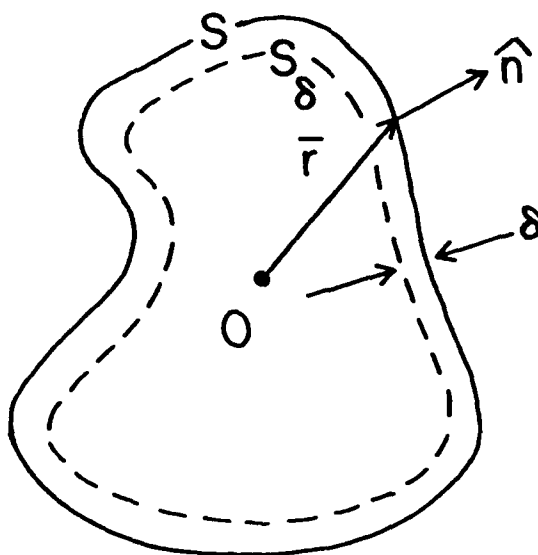


Figure 6. Geometry of Perfect Conductor for Dual-Surface Magnetic-Field Integral Equation

The dual-surface magnetic-field integral equation will have a unique solution for \vec{J} at all real frequencies if α is imaginary and the positive real constant δ is less than approximately $\lambda/2$.

By considering the fields radiated by the solution currents, uniqueness of solution can be shown for the dual-surface magnetic-field integral equation. $\vec{H}_s(\vec{r})$ will be the magnetic field radiated by the solution \vec{J}

$$\vec{H}_s(\vec{r}) = \frac{1}{4\pi} \int_S \vec{J}(\vec{r}') \times \nabla' \psi dS' \quad (\vec{r} \text{ not in } S). \quad (69)$$

If \vec{J} is the unique scattering current for Eq. (64), then $\vec{H}_s(\vec{r}')$ is the correct scattered field for all \vec{r} not in the surface current. Because it is not known that \vec{J} is the correct unique solution, Eq. (64) only defines an unknown magnetic field $\vec{H}_s(\vec{r}')$.

Taking the curl of the curl of Eq. (64) shows that this unknown magnetic field satisfies the homogeneous vector wave equation for all \vec{r} not in the surface current \vec{J} , that is,

$$\nabla \times \nabla \times \vec{H}_s - k^2 \vec{H}_s = 0 \quad (\vec{r} \text{ not in } S). \quad (70)$$

Let \vec{r} approach S in Eq. (64) from the inside of S and using the principal value formula³

$$\int_{S(\vec{r} \rightarrow S)} \nabla' \psi dS' = \oint_S \nabla' \psi dS' - 2\pi \hat{n}, \quad (71)$$

as explained above in the derivation of the magnetic-field integral equation, Eq. (64) can be written as

$$\vec{H}_s(\vec{r}_-) = \frac{1}{4\pi} \int \vec{J}(\vec{r}') \times \nabla' \psi(\vec{r}, \vec{r}') dS' - \hat{n} \times \frac{\vec{J}(\vec{r})}{2} \quad (\vec{r} \text{ on } S), \quad (72)$$

where \vec{r}_- indicates the field evaluated just inside the surface current. Since Eq. (64) is true for all \vec{r} inside S , \vec{H}_s on the parallel surface S_δ can be written as

$$\vec{H}_s(\vec{r} - \delta \hat{n}) = \frac{1}{4\pi} \int \vec{J}(\vec{r}') \times \nabla' \psi(\vec{r} - \delta \hat{n}) dS' \quad (\vec{r} \text{ on } S). \quad (73)$$

Multiply Eq. (73) by α , add to Eq. (72), and then take \hat{n} cross the results to obtain

$$\hat{n} \times [\vec{H}_s(\vec{r}_-) + \alpha \vec{H}_s(\vec{r} - \delta \hat{n})] = \hat{n} \times \frac{1}{4\pi} \int \vec{J}(\vec{r}') \times \nabla' \psi_0(\vec{r}, \vec{r}') dS' - \frac{\vec{J}(\vec{r})}{2} \quad (\vec{r} \text{ on } S). \quad (74)$$

Comparing Eqs. (74) and (65), which \vec{J} must satisfy, shows

$$\hat{n} \times [\vec{H}_s(\vec{r}_-) + \vec{H}_{inc}(\vec{r}) + \alpha \vec{H}_s(\vec{r} - \delta \hat{n}) + \alpha \vec{H}_{inc}(\vec{r} - \delta \hat{n})] = 0 \quad (\vec{r} \text{ on } S). \quad (75)$$

The incident magnetic field must also satisfy the vector wave equation

$$\nabla \times \nabla \times \vec{H}_{inc} - k^2 \vec{H}_{inc} = 0. \quad (76)$$

Adding Eq. (70) to Eq. (76) and rewriting Eq. (76) to arrive at the interior boundary value problem

$$\nabla \times \nabla \times \vec{H} - k^2 \vec{H} = 0 \quad (\vec{r} \text{ inside } S), \quad (77)$$

$$\hat{n} \times [\vec{H}(\vec{r}) + \alpha \vec{H}(\vec{r} - \delta \hat{n})] = 0 \quad (\vec{r} \rightarrow S \text{ from inside}), \quad (78)$$

where $\vec{H}(\vec{r})$ is the total magnetic field given by

$$\vec{H}(\vec{r}) = \vec{H}_{inc}(\vec{r}) + \vec{H}_s(\vec{r}). \quad (79)$$

Now it needs to be shown that the boundary value problem of Eqs. (77) and (78) has only the trivial solution, $\vec{H}(\vec{r}) = 0$, for the total field throughout the volume enclosed by the surface S , provided the constant α is imaginary and the positive real constant δ is smaller than approximately $\lambda/2$. Rewrite the boundary condition Eq. (78) explicitly for the magnetic field tangent to the the surface S to get,

$$\vec{H}_t(\vec{r}) + \alpha \vec{H}_t(\vec{r} - \delta \hat{n}) = 0 \quad (\vec{r} \rightarrow S \text{ from inside}). \quad (80)$$

Rewrite the tangential magnetic fields in Eq. (80) in terms of a magnitude and phase

$$\vec{H}_t(\vec{r}) = |\vec{H}_t(\vec{r})| e^{j\phi(\vec{r})} \quad (\vec{r} \rightarrow S \text{ from inside}), \quad (81)$$

$$\vec{H}_t(\vec{r} - \delta \hat{n}) = [|\vec{H}_t(\vec{r})| + \Delta \vec{H}_t(\vec{r}, \delta)] e^{j[\phi(\vec{r}) + \Delta \phi(\vec{r}, \delta)]} \quad (\vec{r} \rightarrow S \text{ from inside}), \quad (82)$$

where $\Delta \vec{H}_t$ and $\Delta \phi$ are the differences between the magnitudes and the phases of $\vec{H}_t(\vec{r})$ and $\vec{H}_t(\vec{r} - \delta \hat{n})$. Now using Eqs. (81) and (82) in Eq. (80) results in

$$|\vec{H}_t| + \alpha(|\vec{H}_t| + \Delta \vec{H}_t)(\cos \Delta \phi + j \sin \Delta \phi) = 0. \quad (83)$$

Since $|\vec{H}_t|$, $\Delta \vec{H}_t$, and $\Delta \phi$ are real numbers, by letting the constant α be an imaginary number ($j\alpha_j$), we can equate the real and imaginary parts of Eq. (83) separately to give

$$|\vec{H}_t| - \alpha_j(|\vec{H}_t| + \Delta \vec{H}_t) \sin \Delta \phi = 0, \quad (84)$$

and

$$\alpha_j(|\vec{H}_t| + \Delta\vec{H}_t) \cos \Delta\phi = 0. \quad (85)$$

For small δ , $\Delta\phi$ will be small (much less than $\pm 90^\circ$), and thus Eqs. (84) and (85) imply that $|\vec{H}_t| = 0$ and $\Delta\vec{H}_t = 0$, or

$$\vec{H}_t(\vec{r}) = 0 \quad (\vec{r} \rightarrow S \text{ from inside}) \quad (86)$$

$$\vec{H}_t(\vec{r} - \delta\hat{n}) = 0 \quad (\vec{r} \rightarrow S \text{ from inside}). \quad (87)$$

This says that when the constant α is chosen imaginary and δ is not large, the two separate tangential fields in the boundary condition are zero, meaning that the tangential magnetic field on both surfaces is zero.

The boundary condition of Eq. (86) restricts the nonzero solutions of Eq. (77) to the resonant modes of the cavity formed by a perfectly magnetically conducting surface S . These modes form standing waves within the cavity with magnetic and electric fields that can be chosen real and imaginary, respectively.¹³ The tangential magnetic field near the surface can be expressed approximately as

$$\vec{H}_t(\vec{r}_s, r_n) \approx A(\vec{r}_s, r_n) \sin \gamma r_n, \quad (88)$$

where (\vec{r}_s, r_n) are the coordinates tangent and normal to the surface S , γ is a positive real propagation constant with a value equal to or less than the free space constant k , and the amplitude $A(\vec{r}_s, r_n)$ varies with r_n slowly compared to the variation of $\sin \gamma r_n$. If r_n equals zero on S , the boundary condition of Eq. (86) is satisfied by Eq. (88). The boundary condition of Eq. (87) applied to Eq. (88) requires that

$$\gamma\delta = m\pi \quad (89)$$

for m equal to a positive integer. (It is assumed is that there will be some portion of S where A is nonzero.) Since the maximum value of γ is $k = 2\pi/\lambda$, Eq. (89) cannot be satisfied for

$$0 < \delta \lesssim \lambda/2. \quad (90)$$

An approximate sign is included in Eq. (90) because Eq. (88) is an approximate expression for the standing wave field near the surface.

¹³Borgnis, F.E. and Papas, C.H. (1958) Electromagnetic waveguides and resonators, *Encyclopedia of Physics*, S. Flugge, ed., 16: Springer-Verlag, Berlin.

To summarize, the only solution to Eqs. (77) and (78) for α imaginary and $0 < \delta \lesssim \lambda/2$ is the trivial solution, $\vec{H}(\vec{r}) = \vec{H}_{inc}(\vec{r}) + \vec{H}_s(\vec{r}) = 0$ throughout the volume enclosed by S . Since $\vec{E} = -\nabla \times \vec{H}/j\omega\epsilon_0$, the electric field $\vec{E}(\vec{r}) = \vec{E}_{inc}(\vec{r}) + \vec{E}_s(\vec{r})$ within this volume is also identically zero. It can be proved¹² that the current that produces the negative of the incident electromagnetic fields throughout the volume enclosed by S is the correct unique current for the exterior scattering problem. Since this unique solution is derived from the solution current of Eq. (65), the dual-surface magnetic-field integral equation has a unique solution.

The existing magnetic-field integral equation solution is easily modified to obtain the dual-surface magnetic-field integral equation. The values of \vec{H}_{inc} and ψ are now calculated at both the outer surface and an inner surface some distance δ inside. This requires that the computer program be modified to simply evaluate these functions at $\vec{r} - \delta\hat{n}$ as well as at \vec{r} .

For the body of revolution solution, α was chosen to be $j(\sqrt{-1})$ to weight the field on S and S_δ equally in the boundary conditions of Eqs. (77) and (78). To keep the surface S_δ about an equal distance between the two critical values, $\delta = 0$ and $\lambda/2$, δ was selected to equal $\lambda/4$.⁵

4.2 Numerical Results

Figure 7 plots the normalized radar cross section $\sigma/\pi a^2$ in the backscattering direction from the same spherical scatterer, as we did above with the magnetic-field integral equation, using the dual-surface magnetic-field integral equation and the Mie series with the incident wave along the positive z-axis. The spurious resonances are eliminated by use of the dual-surface magnetic-field integral equation, and there is excellent agreement out to $ka \cong 10$. At $ka = 10$, there are five t -segments per wavelength, and as this number of t -segments falls below five per wavelength, the dual-surface magnetic-field integral equation solution rapidly degrades. This is expected because a general rule of thumb for moment method solutions for the magnetic-field integral equations is to have no less than about five segments per wavelength.⁵

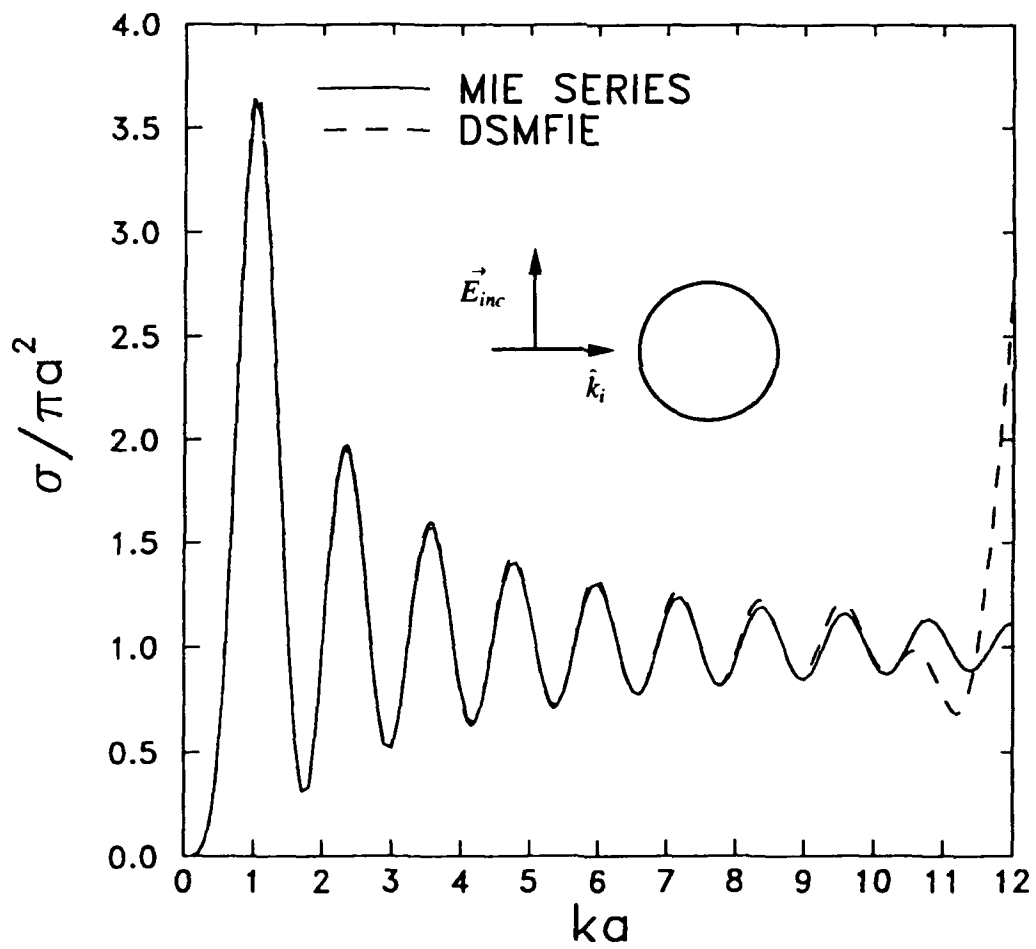


Figure 7. Backscattering Cross Section Versus ka of a Perfectly Conducting Sphere Computed with the Dual-Surface Magnetic-Field Integral Equation and the Mie Series

Figure 8 shows the comparison of the Mie series, dual-surface magnetic-field integral equation, and the combined-field integral equation⁶ for the same spherical model with the incident wave along the positive z -axis. The dual-surface magnetic-field integral equation and combined-field integral equation are in good agreement up to $ka = 5$ (ten segments per wavelength) where the combined-field integral equation starts to deviate from the Mie series solution. As stated previously, the dual-surface magnetic-field integral equation does not show a significant deviation until $ka \cong 10$. The computer run times for the dual-surface magnetic-field integral equation and combined-field integral equation were approximately equal for the spherical model with the same number of patches per wavelength. However, the dual-surface magnetic-field integral equation requires less segments per wavelength for the same accuracy.

The dual-surface magnetic-field integral equation solution was computed as a function of bistatic angle for a sphere of $ka = 20$ with the incident field along the positive z -axis. This result was compared with the Mie series solution, and again the agreement is excellent as seen in Figures 9 and 10.

To ensure that an adequate number of modes are being calculated, according to the criterion of Eq. (63), the same spherical model was used and the incident field was moved to the positive x -axis. Figures 11 and 12 show the comparison of the dual-surface magnetic-field integral equation and the Mie series. Again, the agreement is excellent.

To verify the accuracy of the solution for bodies large with respect to wavelength, the cross section of a sphere with $ka = 70$ with the incident field coming in along the positive z -axis was also computed. These results are summarized in Figures 13 and 14. Due to a limitation on computer time, however the case of the same sphere with the incident field along the positive x -axis was not computed. An attempt was also made to obtain a result from the combined-field integral equation with the incident field along the positive x -axis for a sphere with $ka = 20$, but this was unfruitful. The results obtained were meaningless, but the reason for this is unclear.

Although the sphere results show that the dual-surface magnetic-field integral equation solution appears to work well for a sphere, results from other geometries would increase the confidence in its answers. Wang⁷ plotted the results of plane wave scattering from rotationally symmetric conducting bodies computed from a wire-mesh code. A copy of the code was obtained and several cases presented in Reference 7 were run. Figures 15-24 compare the results of the dual-surface magnetic-field integral equation and the Ohio State code applied to truncated and flat-back cones and the circular cylinder. The radar cross section was calculated as a function of bistatic angle for incident plane waves along the positive and negative z -axes, respectively.

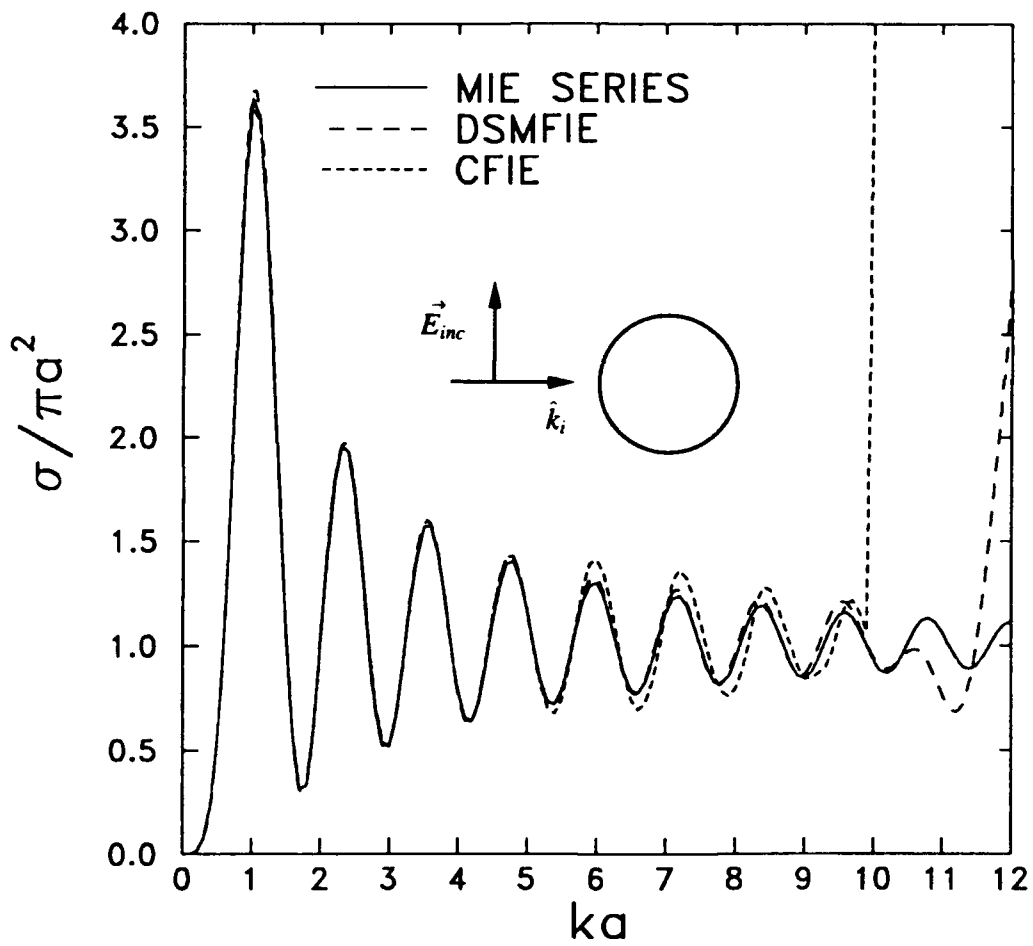


Figure 8. Backscattering Cross Section Versus ka of a Perfectly Conducting Sphere Computed with the Dual-Surface Magnetic-Field Integral Equation, Combined-Field Integral Equation, and the Mie Series

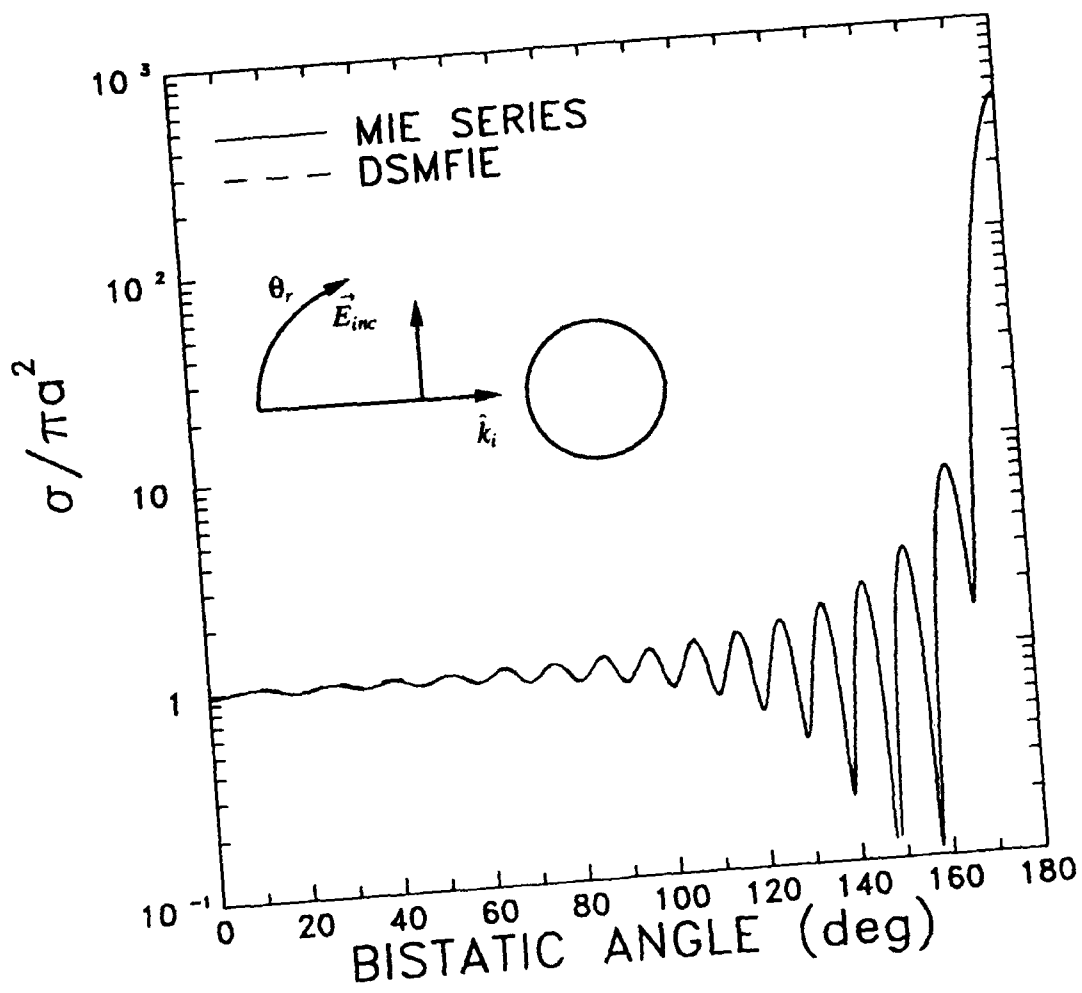


Figure 9. Radar Cross Section Versus Bistatic Angle of a Perfectly Conducting Sphere Computed with the Dual-Surface Magnetic-Field Integral Equation and the Mie Series; $ka = 20$, $\theta_i = 0$, E-Plane

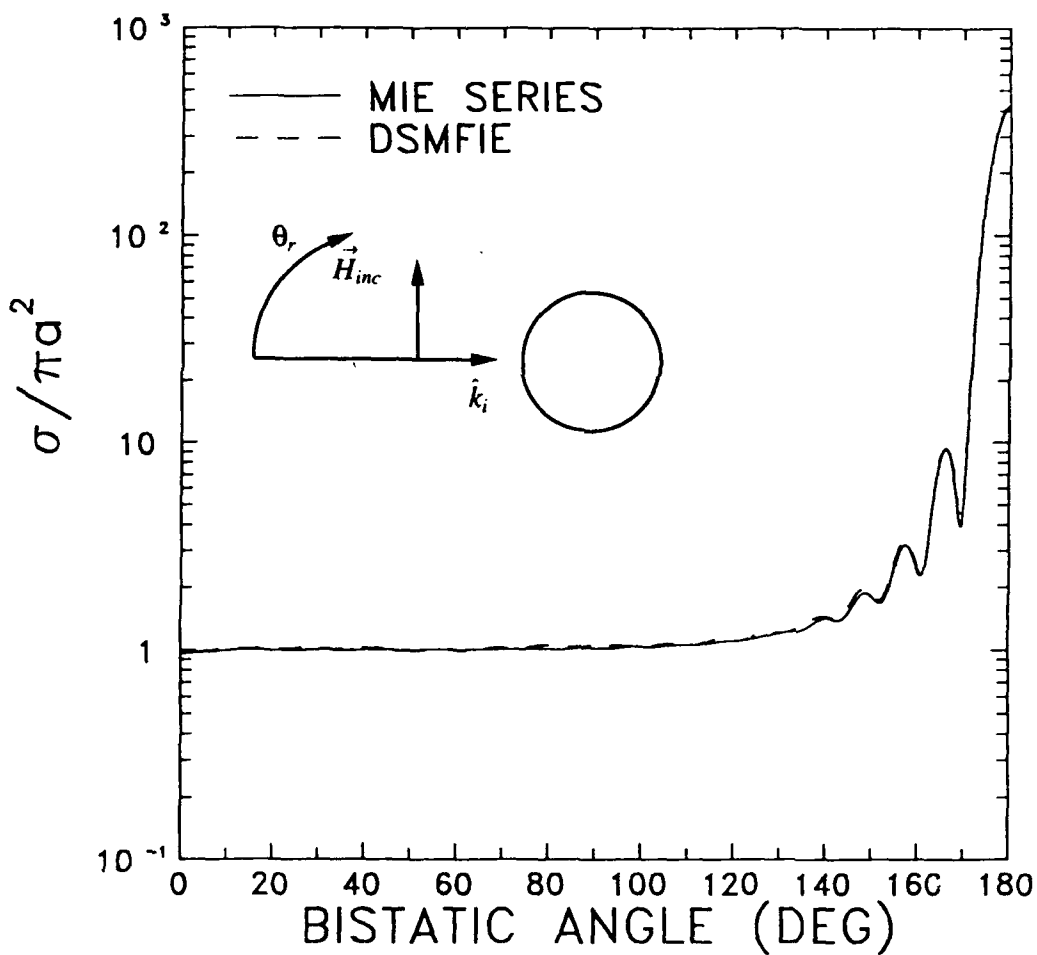


Figure 10. Radar Cross Section Versus Bistatic Angle of a Perfectly Conducting Sphere Computed with the Dual-Surface Magnetic-Field Integral Equation and the Mie Series; $ka = 20$, $\theta_i = 0$, H-Plane

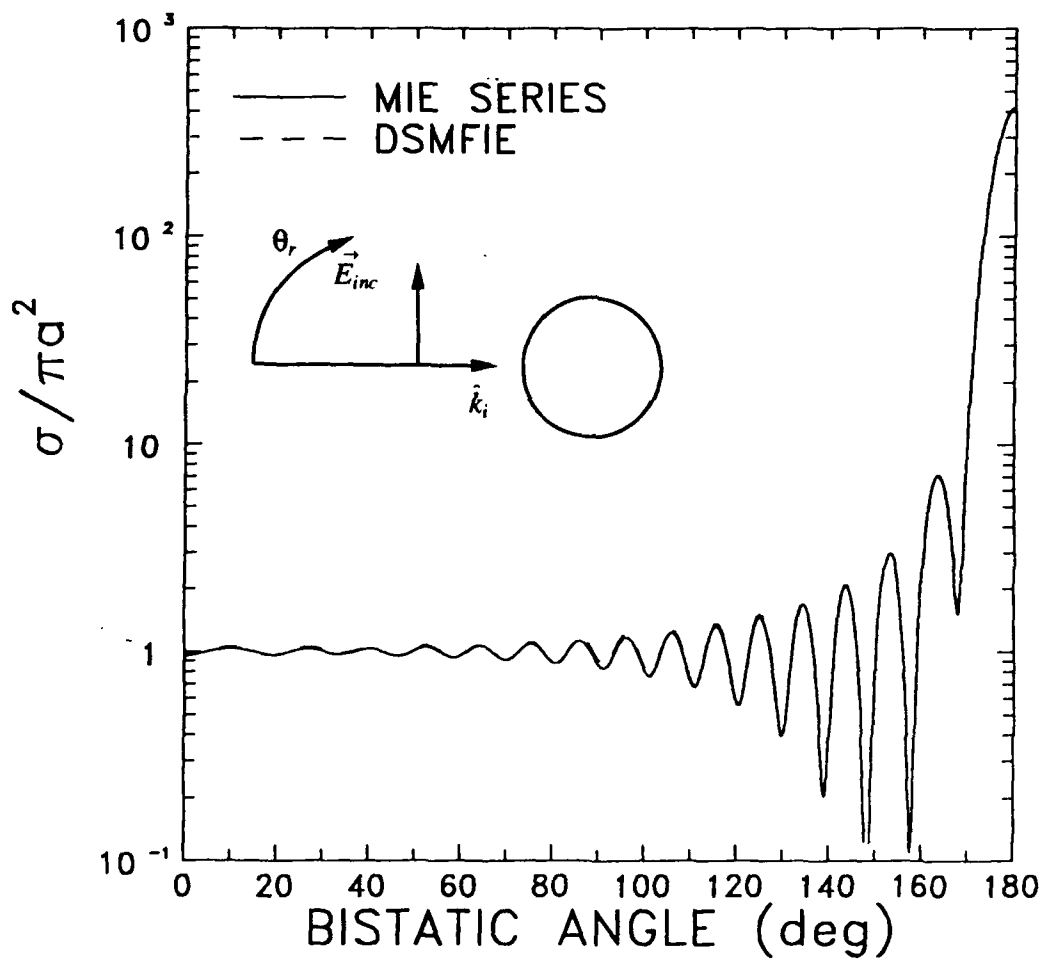


Figure 11. Radar Cross Section Versus Bistatic Angle of a Perfectly Conducting Sphere Computed with the Dual-Surface Magnetic-Field Integral Equation and the Mie Series; $ka = 20$, $\theta_i = 90$, E-Plane

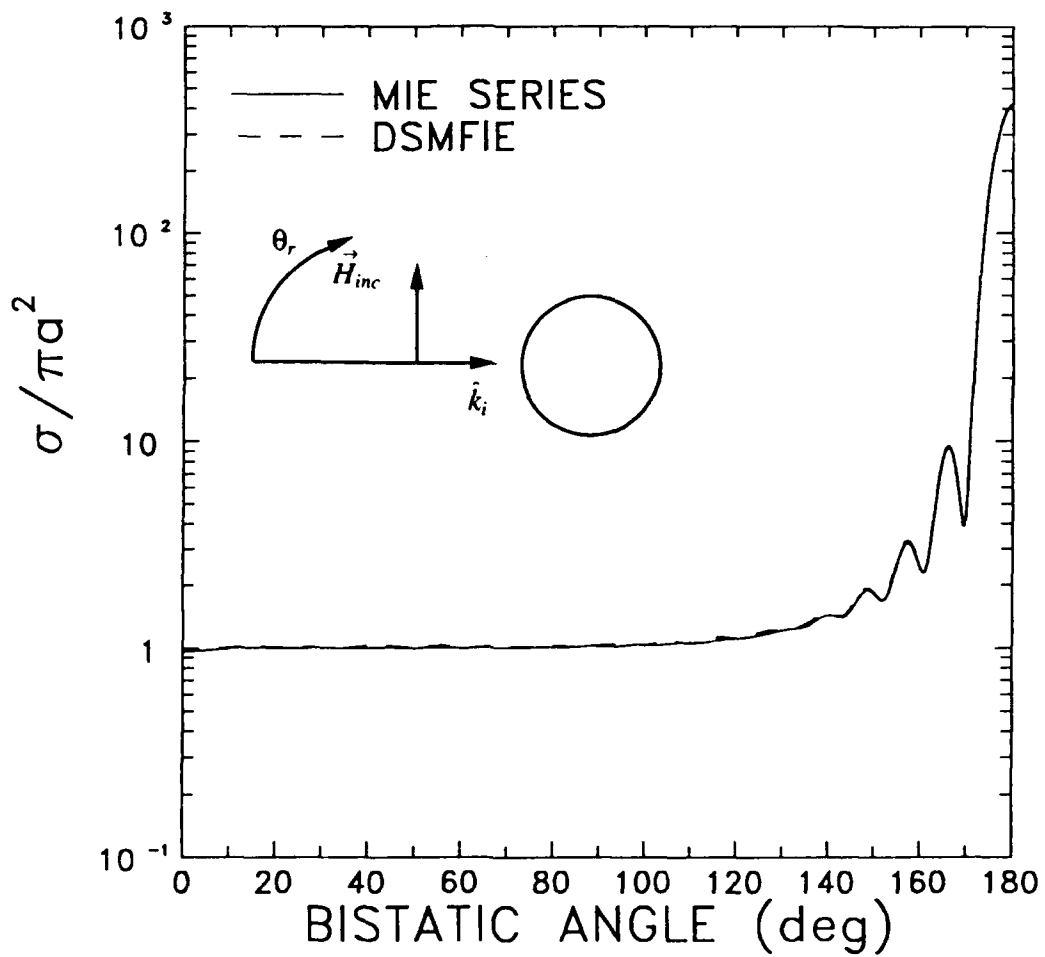


Figure 12. Radar Cross Section Versus Bistatic Angle of a Perfectly Conducting Sphere Computed with the Dual-Surface Magnetic-Field Integral Equation and the Mie Series; $ka = 20$, $\theta_i = 90$, H-Plane

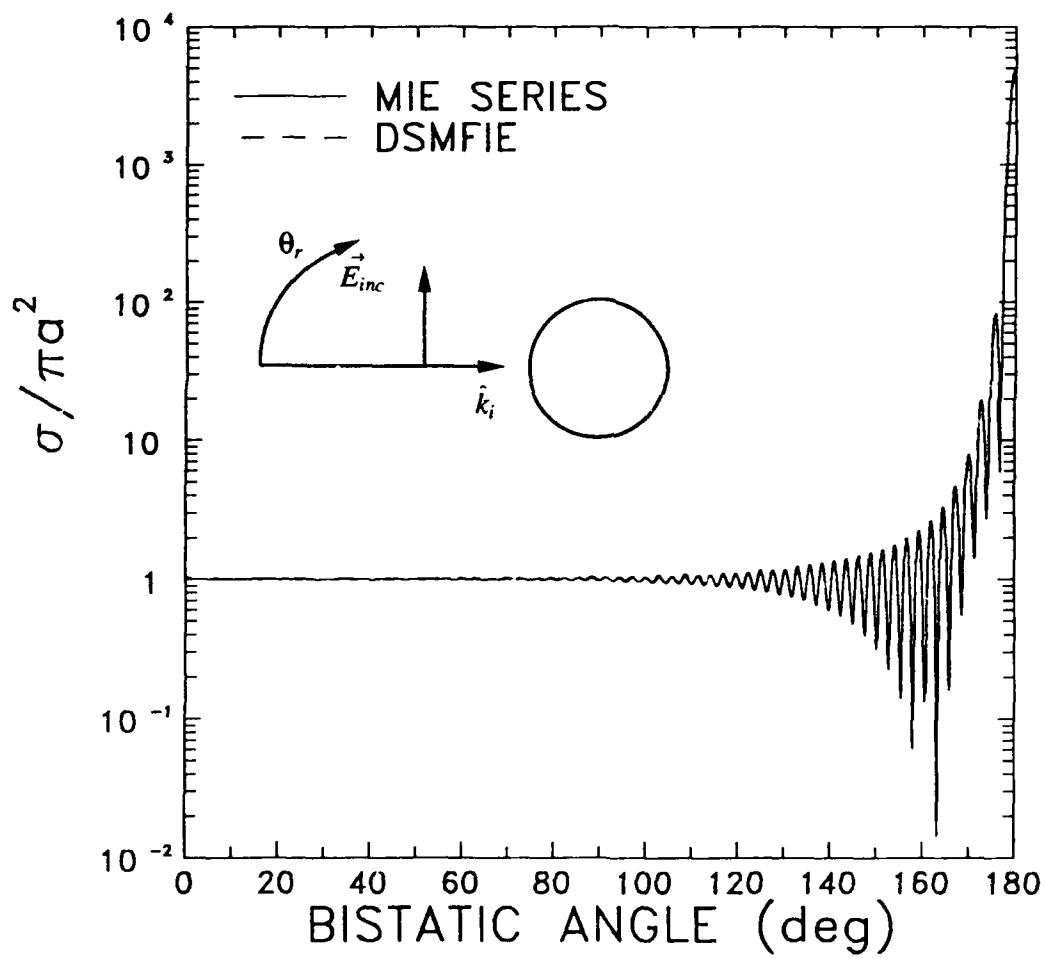


Figure 13. Radar Cross Section Versus Bistatic Angle of a Perfectly Conducting Sphere Computed with the Dual-Surface Magnetic-Field Integral Equation and the Mie Series; $ka = 70$, $\theta_i = 0$, E-Plane

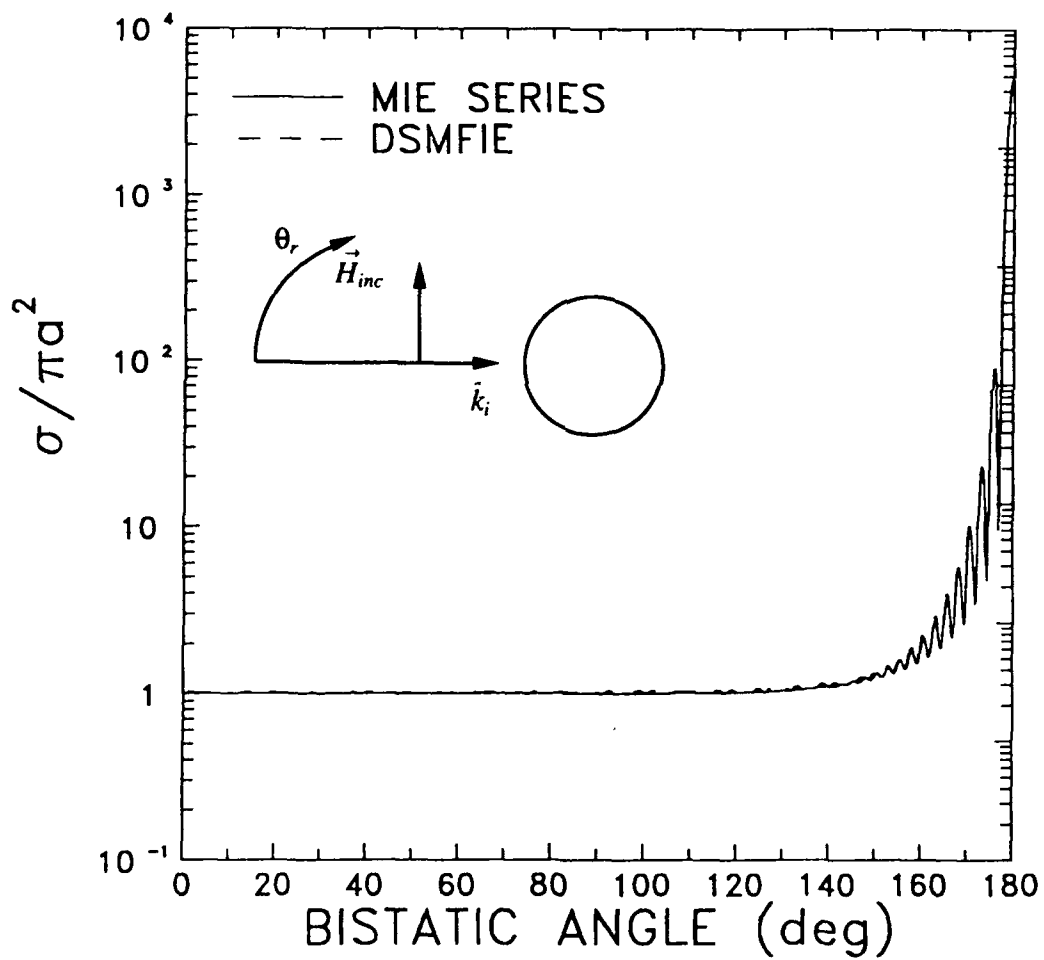


Figure 14. Radar Cross Section Versus Bistatic Angle of a Perfectly Conducting Sphere Computed with the Dual-Surface Magnetic-Field Integral Equation and the Mie Series; $ka = 70$, $\theta_i = 0$, H-Plane

Figures 15 and 16 show no significant difference in the results of the dual-surface magnetic-field integral equation and OSU code for the circular cylinder. As the circular cylinder's radar cross section is identical for the incident wave along the positive z -axis and the negative z -axis as a function of bistatic angle, only the case of the incident wave along the positive z -axis is shown.

Figures 17-20 show the results of the truncated flat-back cone. The E-plane results for the two codes again show no significant difference. The H-plane results have slight deviations of up to 1 dB but are almost identical for the whole range of bistatic angles.

The results for the flat-back cone are shown in Figures 21-24. The maximum difference in the results for the E-plane is approximately 3dB. This occurs for the incident wave along the positive z -axis from about 135 to 140 degrees bistatic angle. The E-plane results for the incident field along the negative z -axis are in excellent agreement showing differences of a fraction of a dB. The difference in the H-plane results for the flat-back cone are the opposite of the E-plane results. There is less than a 0.5 dB difference for the incident field along the positive z -axis and a maximum of 3 dB difference from 40 to 110 degrees bistatic angle for the incident field along the negative z -axis.

Overall there is good agreement between the two codes. Figure 25 shows the results from the OSU code for a circular cylinder for backscatter versus ka where a is the radius and one-half the length of the cylinder. As ka increases, both the length and diameter of the cylinder change appropriately. It is seen that the OSU code has spurious resonances like the magnetic-field integral equation solution. These spurious resonances may be the reason for the difference in the results of the two codes.

Another reason may be the difference method used to approximate the currents on the body with the OSU code using wire-segments and the dual-surface magnetic-field integral equation solution using patches. The results for the dual-surface magnetic-field integral equation were obtained using ten segments per wavelength and the OSU code with 11.8 segments per wavelength. Figure 26 shows the comparison of the results for the OSU code for the flat-backed cone using 10.0 and 11.8 segments per wavelength. There is a 1 dB difference in the two results at backscatter. This seems to indicate that the dual-surface magnetic-field integral equation has increased accuracy over the OSU code for the same number of segments per wavelength as the results from the two codes show little difference if the OSU code uses 11.8 segments per wavelength.

Figures 27 and 28 show the E-plane and H-plane monostatic scattering from a circular cylinder respectively. The measurements were performed at the Rome Laboratory's electromagnetic experimental scattering facility. The results for both polarizations show a difference of approximately 1.5 dB at the specular angles. Modifying the measured values by the difference of the physical optics approximation and the measurements at the specular angles

would produce excellent agreement for the E-plane results. A larger difference in the H-plane results would be due to experimental error, as is demonstrated by the lack of symmetry in the measured results. The experimental error for the measurements is ± 1.5 dB and the difference between the measurements and predicted values are within these bounds. For monostatic results, the body of revolution code must compute a new current solution at every observation angle. The results for the circular cylinder with a radius of 1.2675λ and a length of 6λ required 72 hours of CPU time on a VAX6000. This enormous amount of computer time prevented the comparison of the dual-surface magnetic-field integral equation with other measured monostatic results.

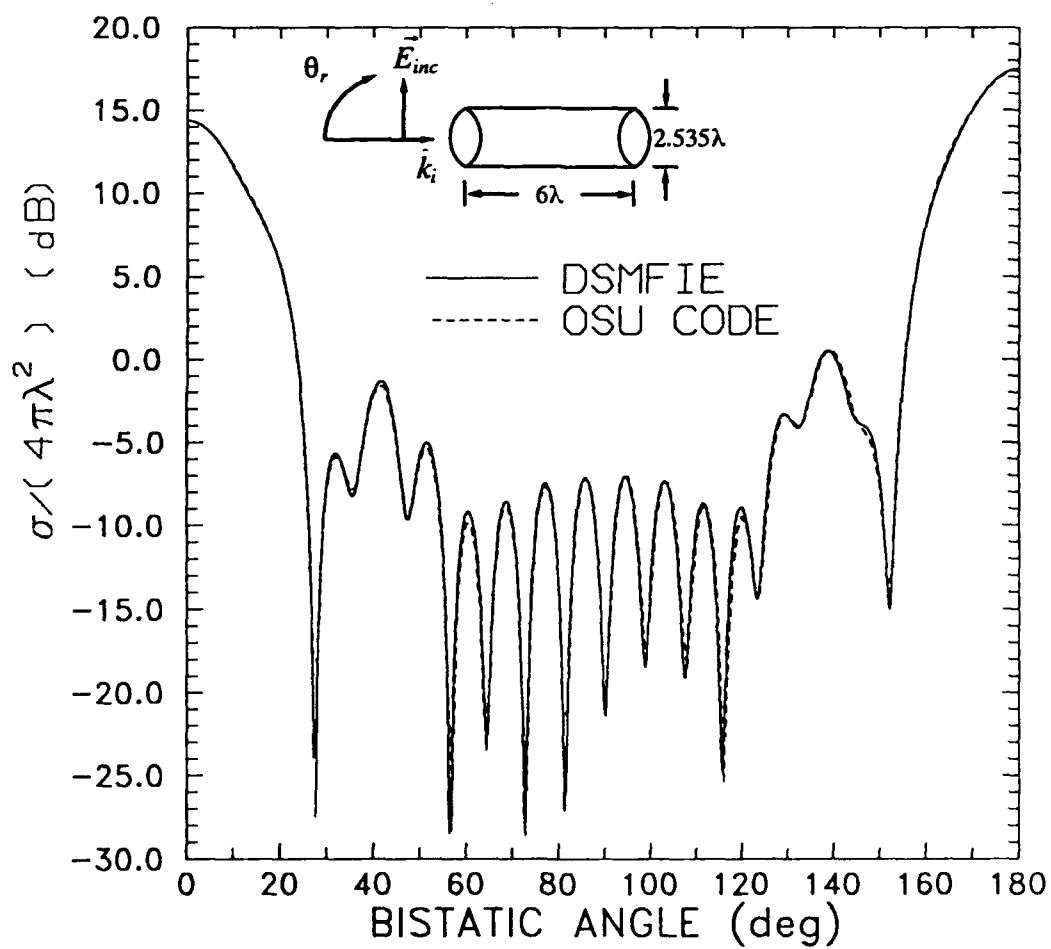


Figure 15. Radar Cross Section Versus Bistatic Angle of a Perfectly Conducting Circular Cylinder Computed with the Dual-Surface Magnetic-Field Integral Equation and the OSU Code; $\theta_i = 0$, E-Plane

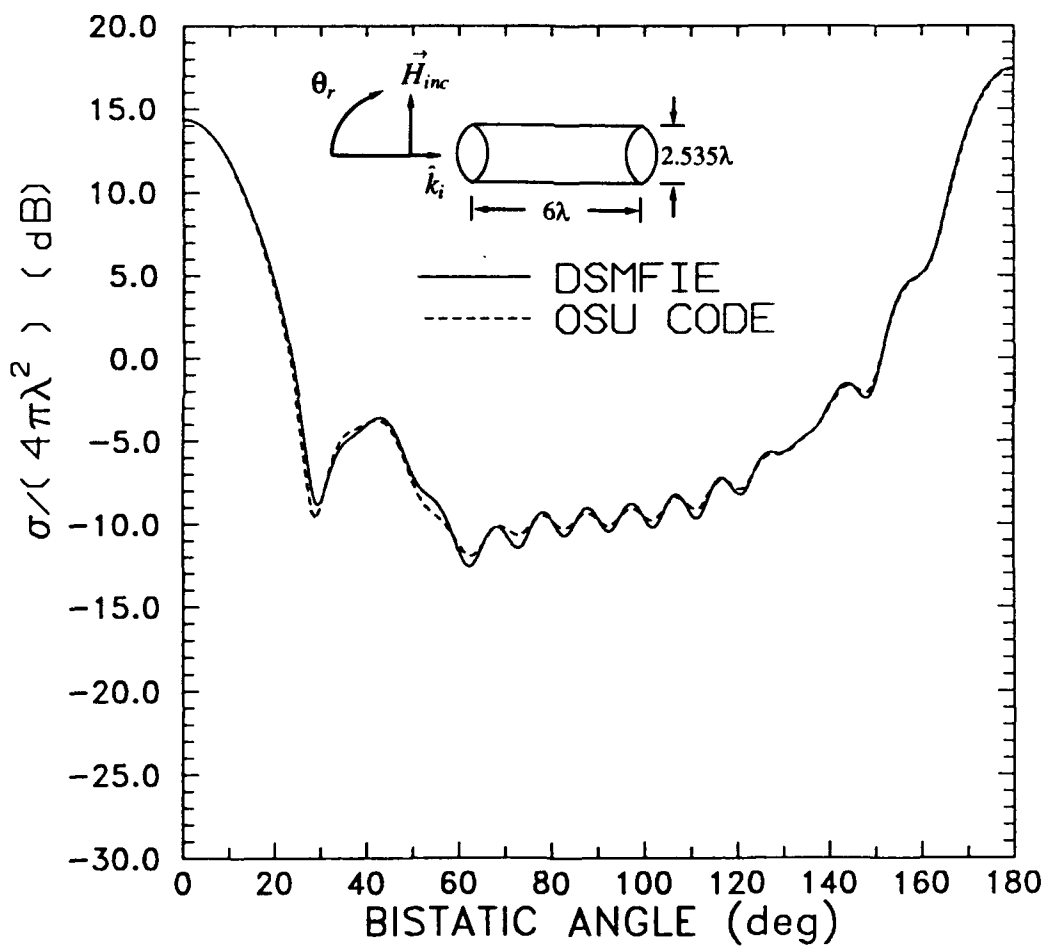


Figure 16. Radar Cross Section Versus Bistatic Angle of a Perfectly Conducting Circular Cylinder Computed with the Dual-Surface Magnetic-Field Integral Equation and the OSU Code; $\theta_t = 0$, H-Plane

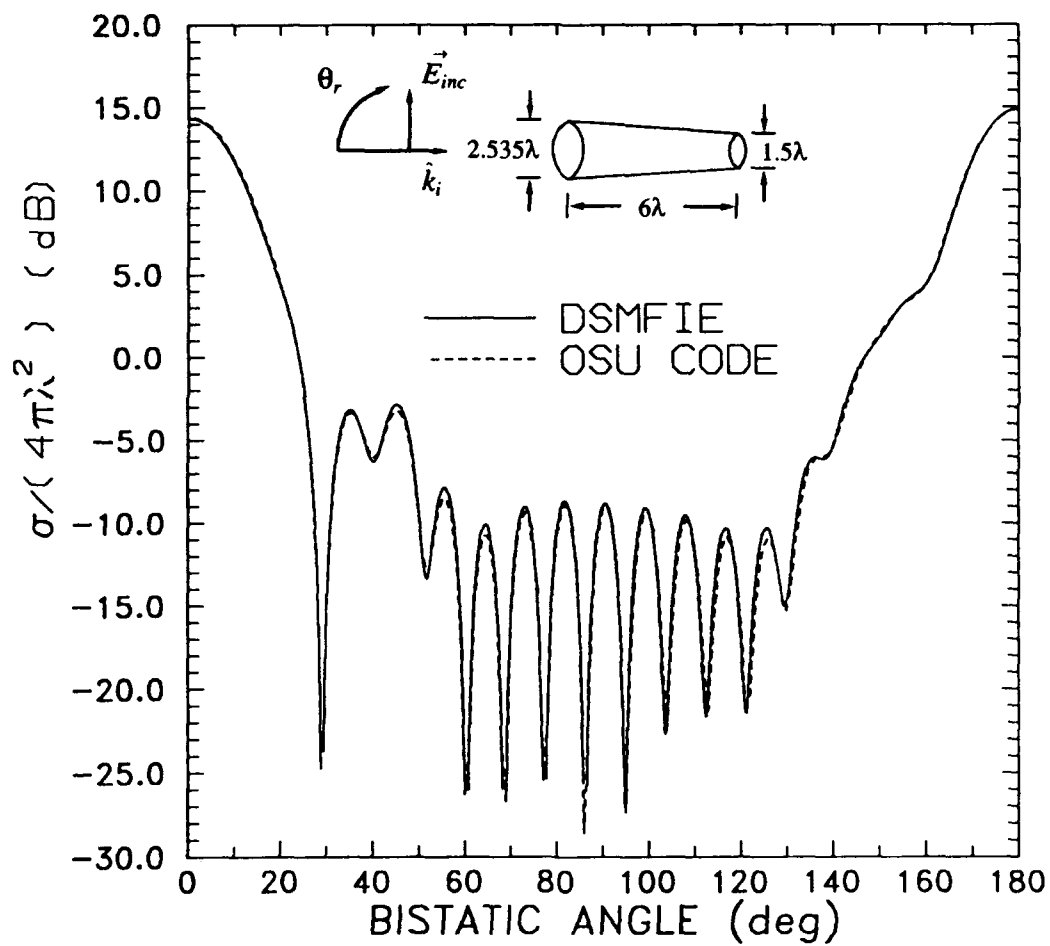


Figure 17. Radar Cross Section Versus Bistatic Angle of a Perfectly Conducting Frustum Computed with the Dual-Surface Magnetic-Field Integral Equation and the OSU Code; $\theta_i = 0$, E-Plane

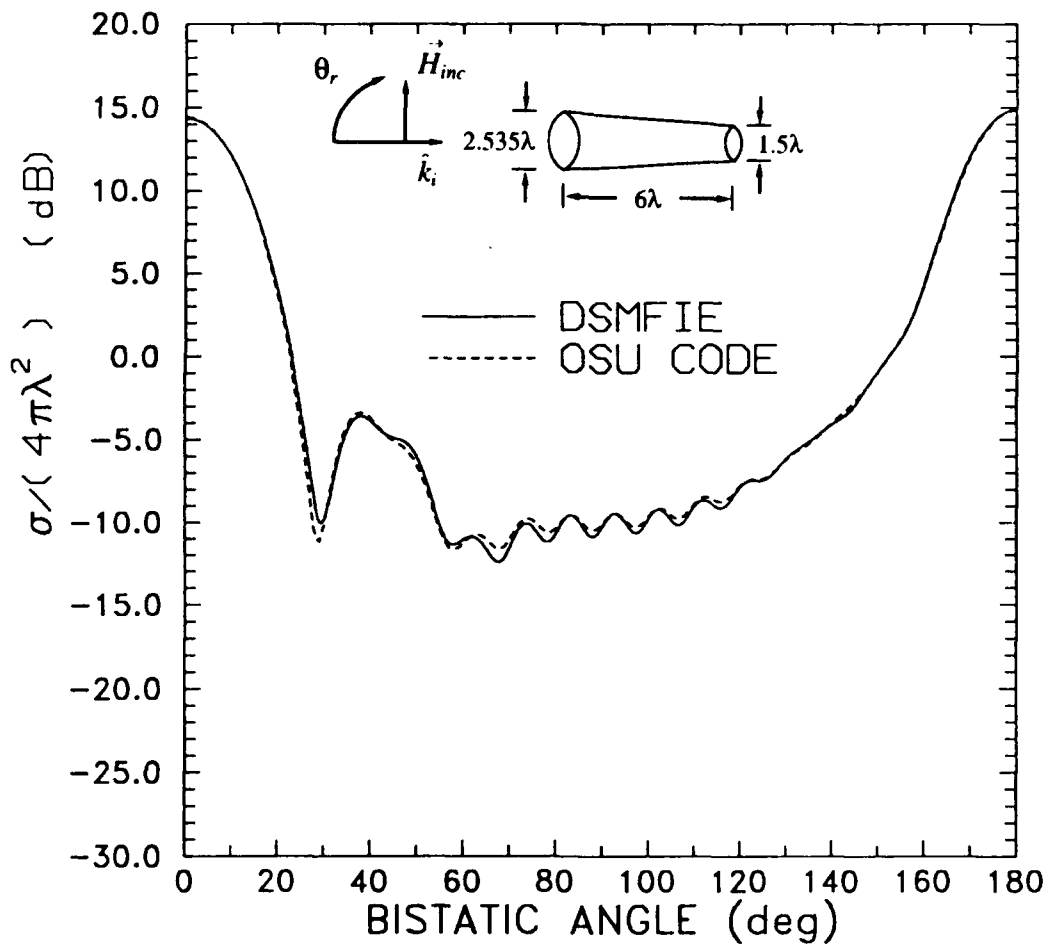


Figure 18. Radar Cross Section Versus Bistatic Angle of a Perfectly Conducting Frustum Computed with the Dual-Surface Magnetic-Field Integral Equation and the OSU Code; $\theta_i = 0$, H-Plane

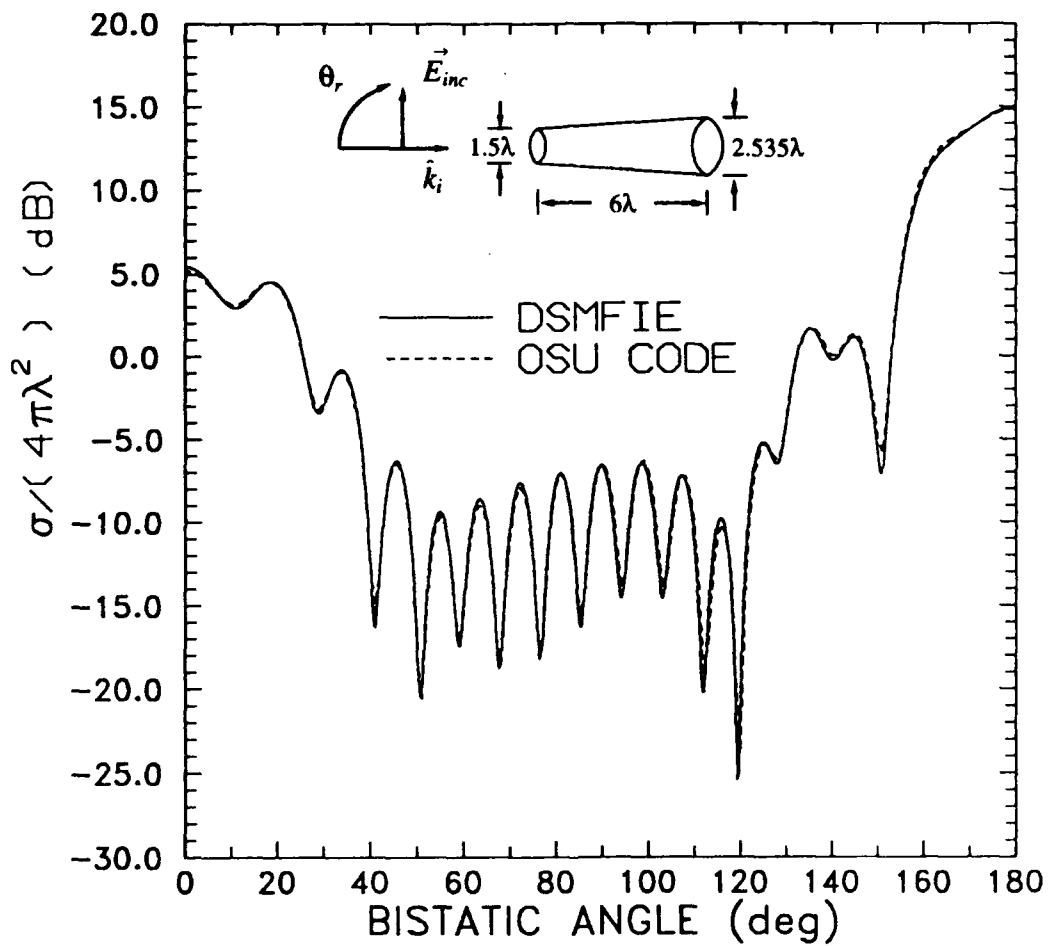


Figure 19. Radar Cross Section Versus Bistatic Angle of a Perfectly Conducting Frustum Computed with the Dual-Surface Magnetic-Field Integral Equation and the OSU Code; $\theta_i = 180$, E-Plane

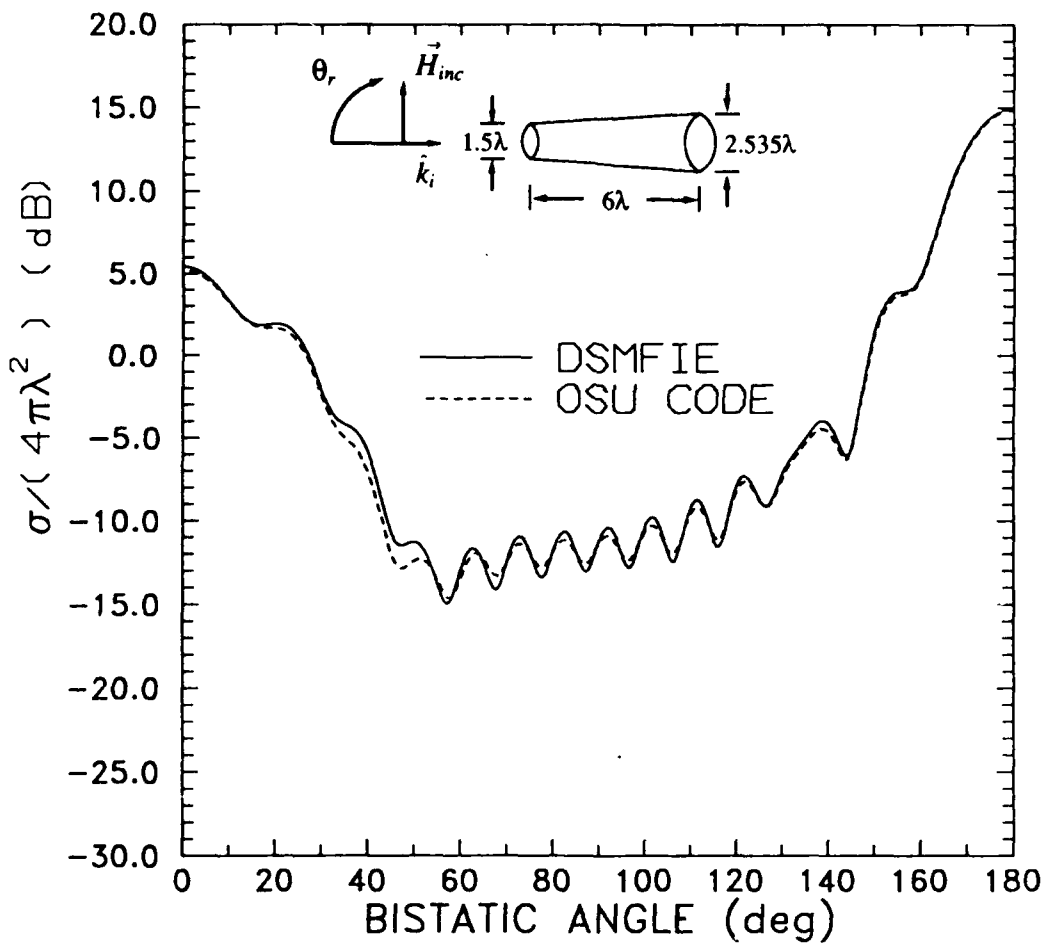


Figure 20. Radar Cross Section Versus Bistatic Angle of a Perfectly Conducting Frustum Computed with the Dual-Surface Magnetic-Field Integral Equation and the OSU Code; $\theta_t = 180$, H-Plane

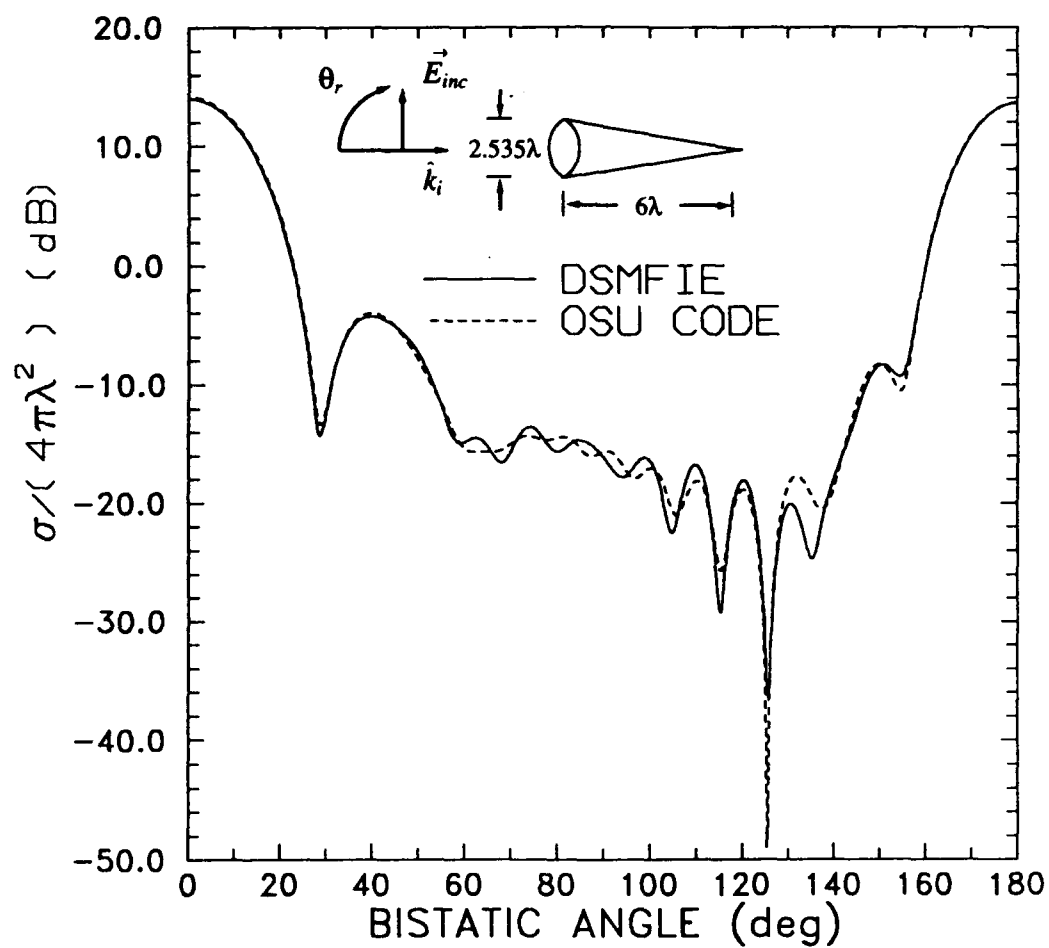


Figure 21. Radar Cross Section Versus Bistatic Angle of a Perfectly Conducting Flat-Backed Cone Computed with the Dual-Surface Magnetic-Field Integral Equation and the OSU Code; $\theta_t = 0$, E-Plane

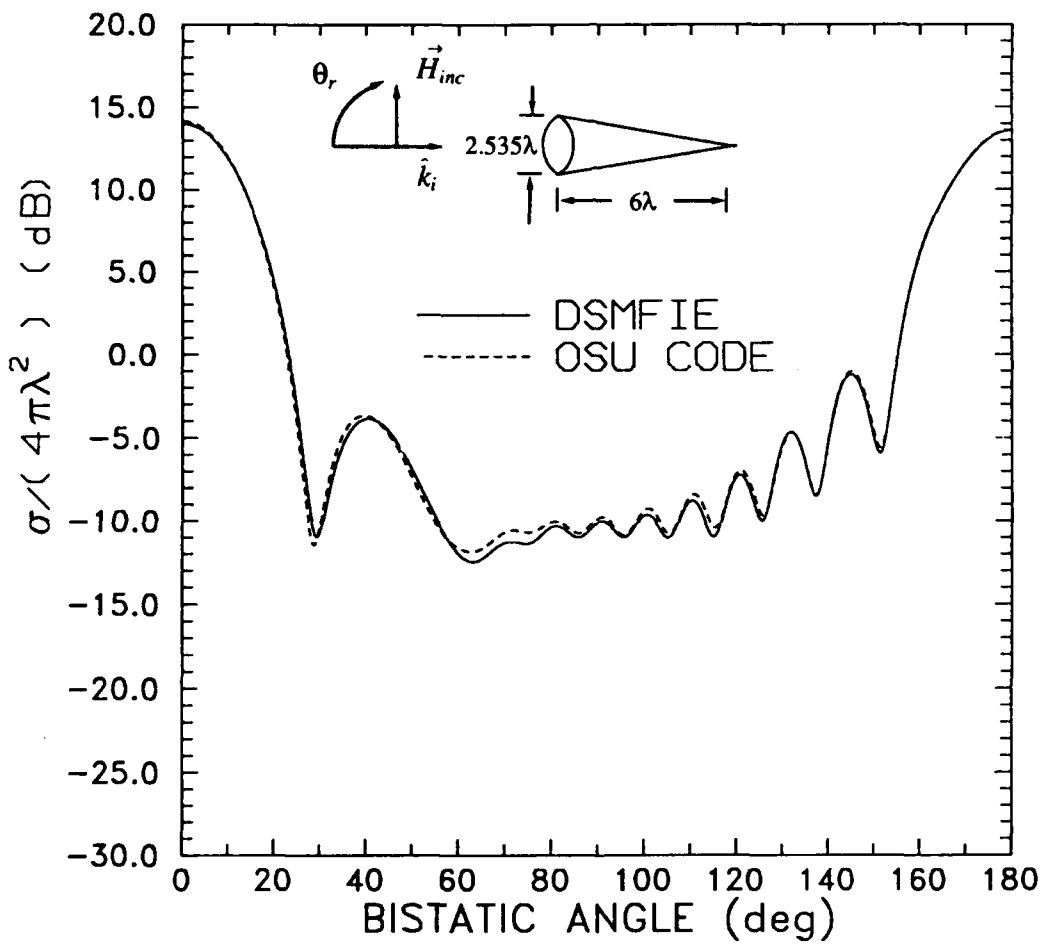


Figure 22. Radar Cross Section Versus Bistatic Angle of a Perfectly Conducting Flat-Backed Cone Computed with the Dual-Surface Magnetic-Field Integral Equation and the OSU Code; $\theta_t = 0$, H-Plane

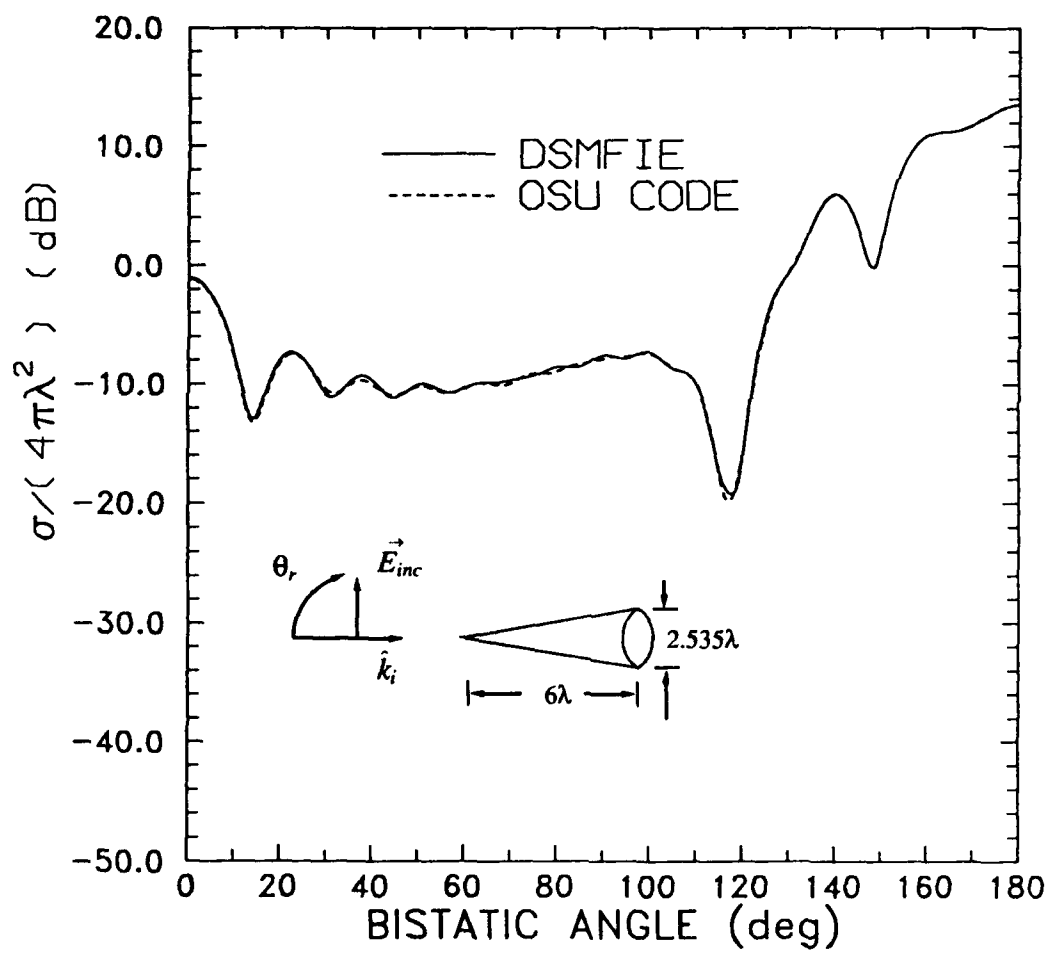


Figure 23. Radar Cross Section Versus Bistatic Angle of a Perfectly Conducting Flat-Backed Cone Computed with the Dual-Surface Magnetic-Field Integral Equation and the OSU Code; $\theta_i = 180$, E-Plane

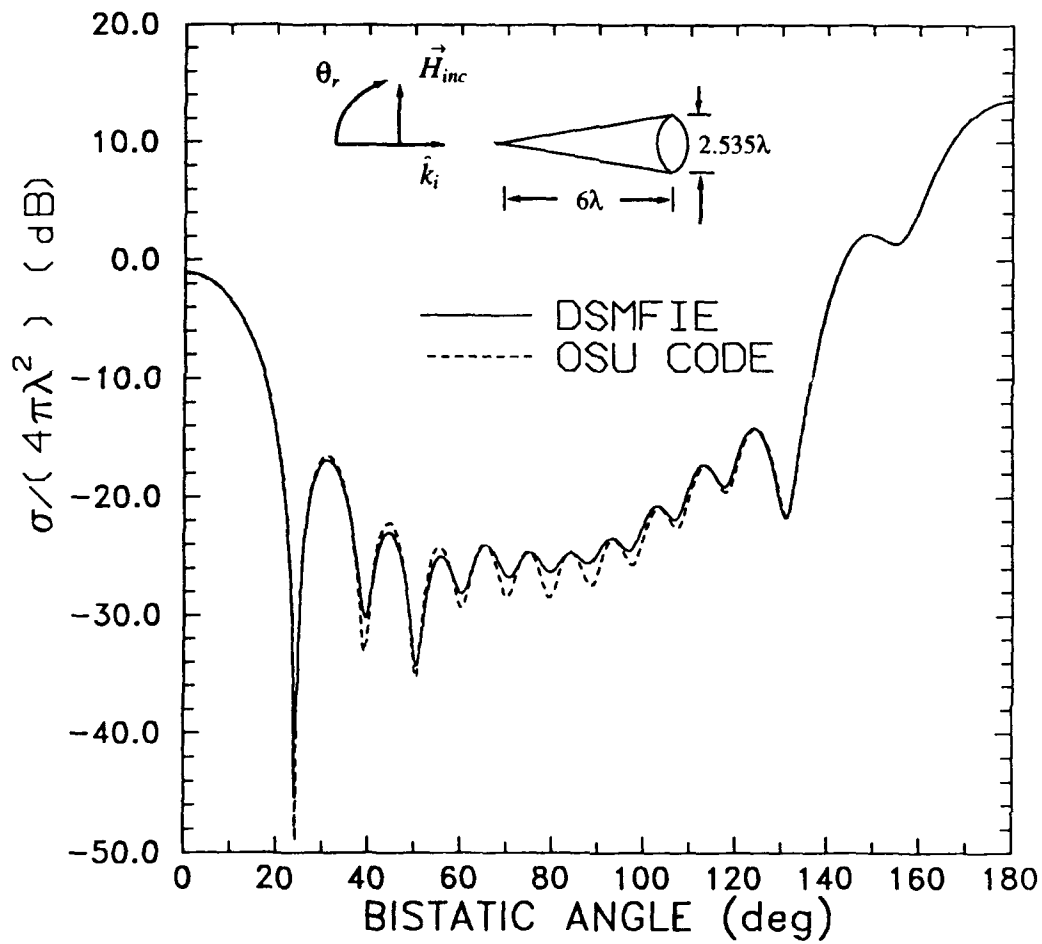


Figure 24. Radar Cross Section Versus Bistatic Angle of a Perfectly Conducting Flat-Backed Cone Computed with the Dual-Surface Magnetic-Field Integral Equation and the OSU Code; $\theta_t = 180$, H-Plane

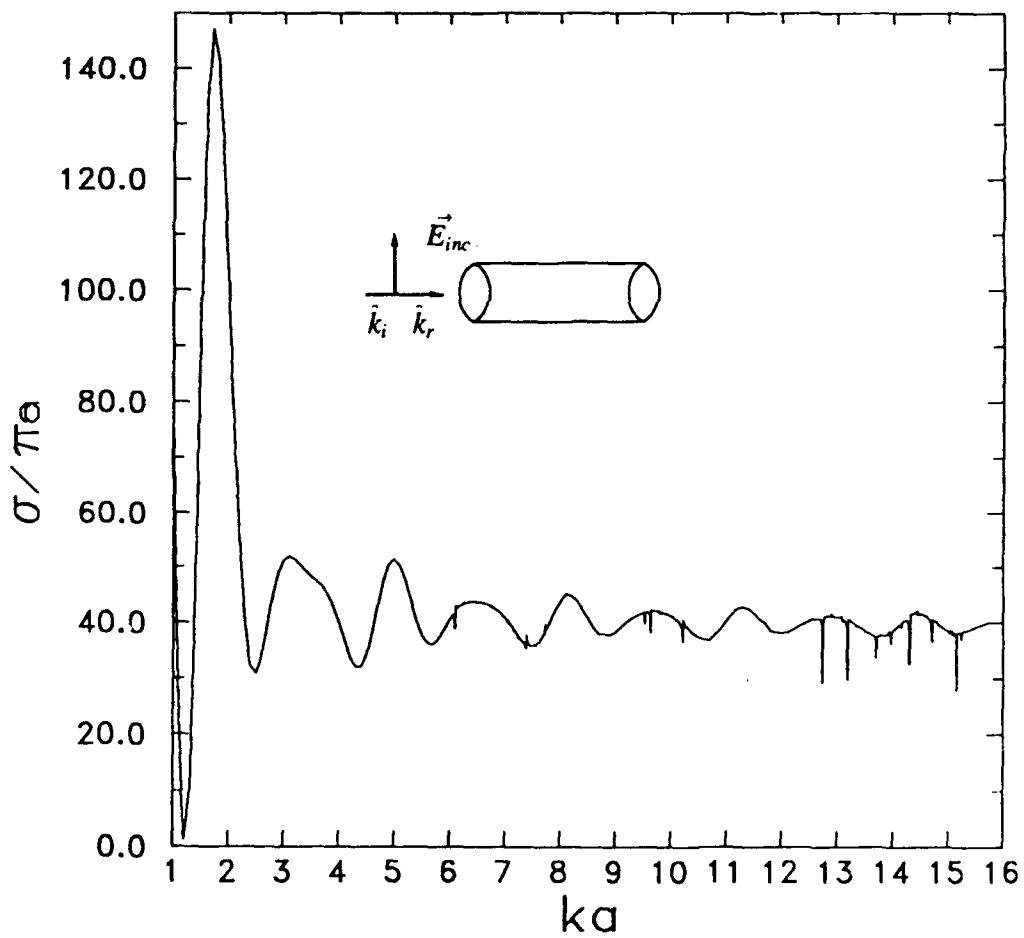


Figure 25. Backscattering Cross Section Versus ka of a Perfectly Conducting Circular Cylinder as Computed with the OSU Code; E-Plane

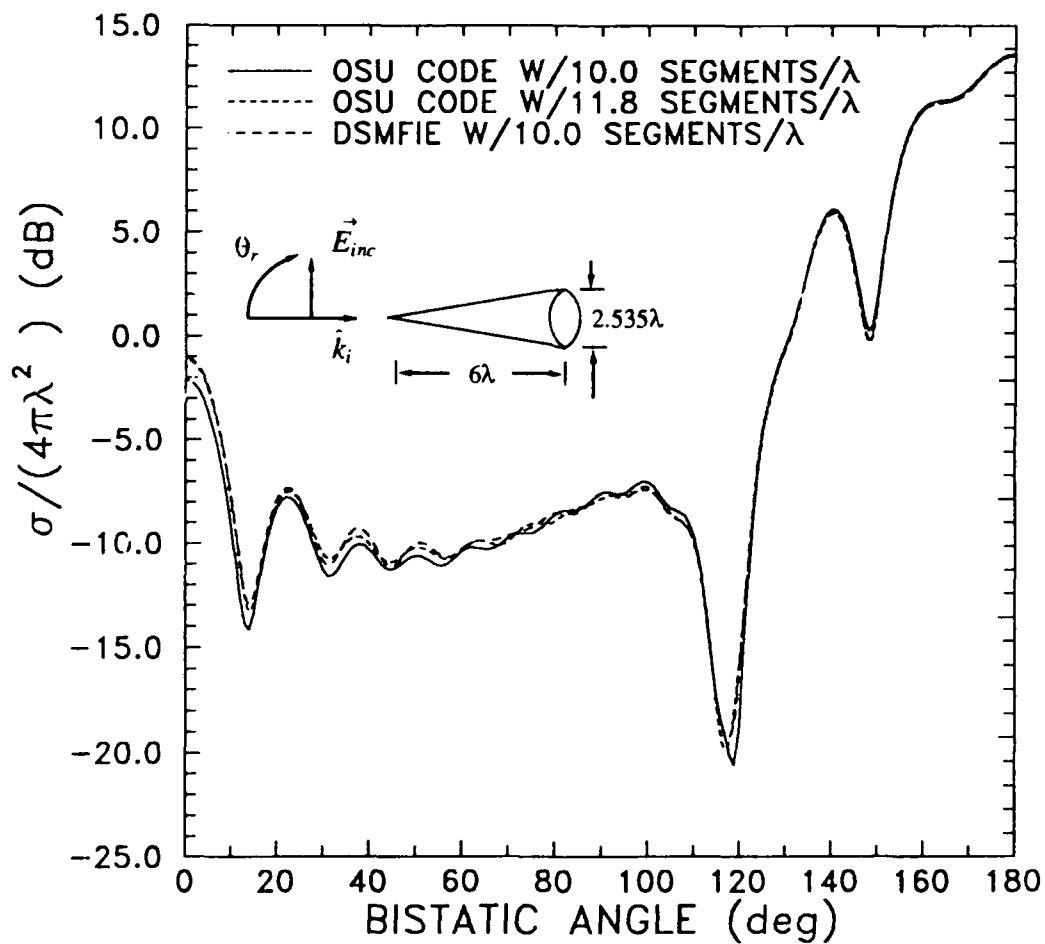


Figure 26. Radar Cross Section Versus Bistatic Angle of a Perfectly Conducting Flat-Backed Cone Computed with the Dual-Surface Magnetic-Field Integral Equation (10.0 Segments Per Wavelength) and the OSU Code (10.0 and 11.8 Segments Per Wavelength); $\theta_t = 180$, E-Plane

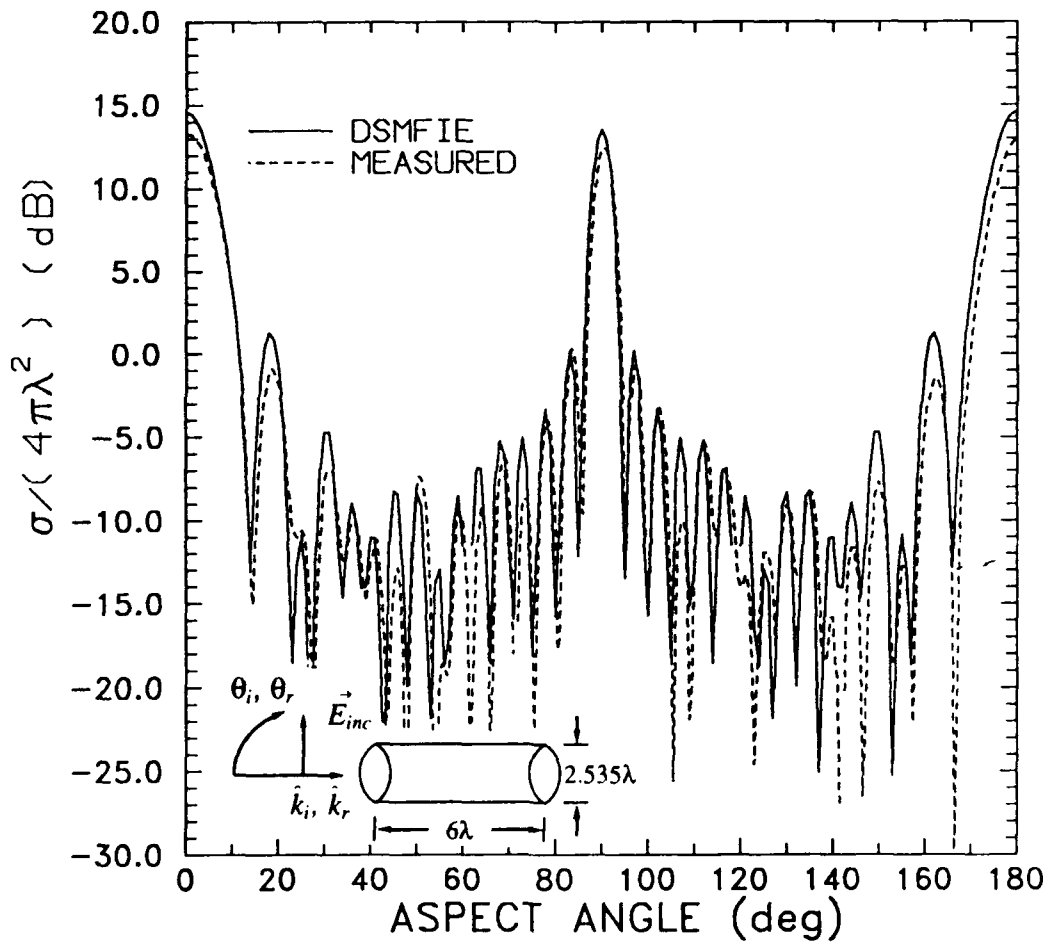


Figure 27. Backscattering Cross Section Versus Aspect Angle of a Perfectly Conducting Circular Cylinder as Computed with the Dual-Surface Magnetic-Field Integral Equation and Measurements; E-Plane

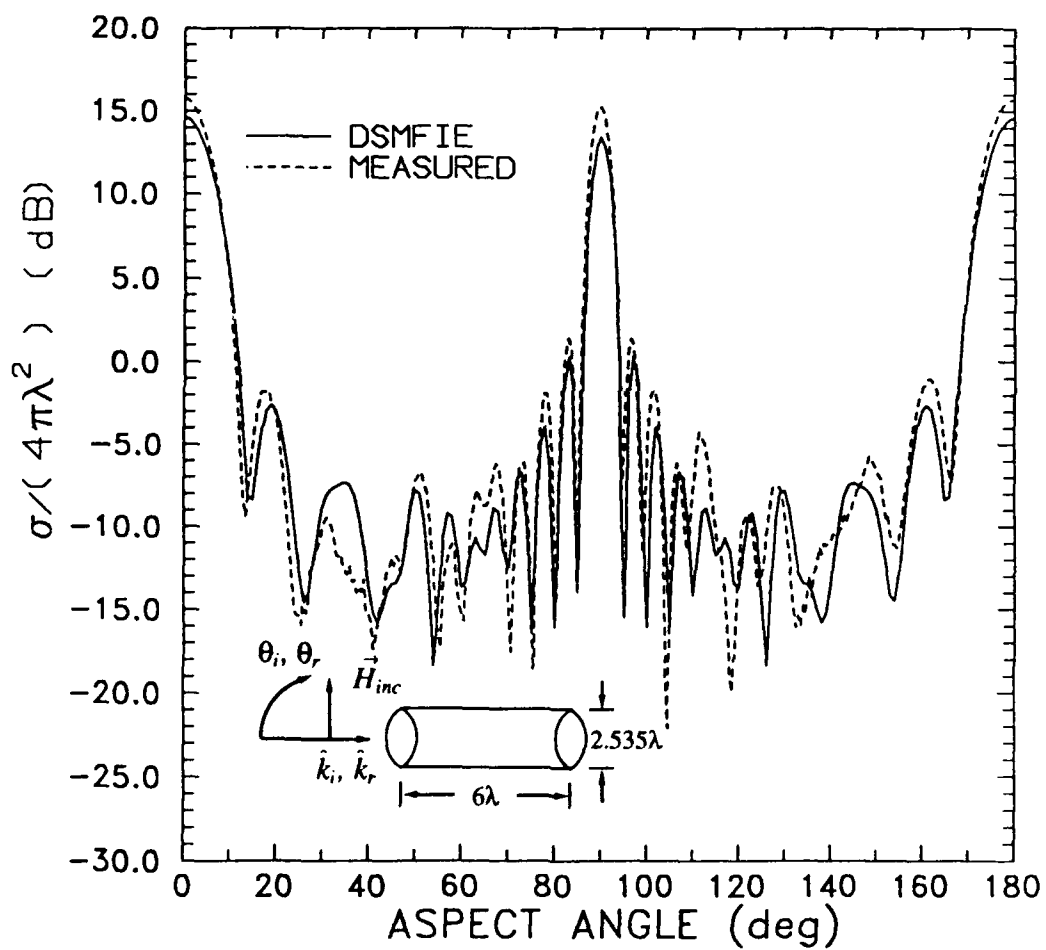


Figure 28. Backscattering Cross Section Versus Aspect Angle of a Perfectly Conducting Circular Cylinder as Computed with the Dual-Surface Magnetic-Field Integral Equation and Measurements; H-Plane

5. CONCLUSIONS

It has been demonstrated that the dual-surface magnetic-field integral equation eliminates the spurious resonances associated with the magnetic-field integral equation for plane wave scattering from bodies of revolution. It was an extremely simple modification to convert the original magnetic-field integral equation computer program to the dual-surface magnetic-field integral equation program. As the magnetic-field integral equation is very well behaved, simple pulse basis and impulse testing functions provide excellent results for as few as five segments per wavelength.

The accuracy of the dual-surface magnetic-field integral equation was shown to be equal or better than the accuracy of the combined-field integral equation for a perfectly conducting sphere. The combined-field integral equation incorporates both the magnetic-field integral equation and the electric-field integral equation, which requires more complicated basis and testing functions for accurate results. These more complicated functions, along with the necessity to incorporate the the electric-field integral equation, make the combined-field integral equation solution more difficult to program than the dual-surface magnetic-field integral equation solution. Even with the more complicated basis and testing functions, the combined-field integral equation started to decrease significantly in accuracy below ten segments per wavelength. This was not true for the dual-surface magnetic-field integral equation. The computer run-times of the two solutions were approximately equal for the perfectly conducting sphere for equal number of segments per wavelength.

The dual-surface magnetic-field integral equation results were also in good agreement with results produced by a wire-mesh body of revolution code.⁷ The results were identical for a circular cylinder but deviated by as much as 3 dB for the truncated and flat-back cones. The differences in the two results may be due to the different methods used to approximate the current on a solid surface and the fact that the OSU code does not eliminate the spurious resonances.

The comparison of the measurements with the dual-surface magnetic-field integral equation results for a circular cylinder also were quite good, demonstrating that the dual-surface magnetic-field integral equation computes accurate results over a wide range of incident angles. The difference in the results from the two different polarizations were within the limits of experimental error. Due to the excessive computer run time required to obtain these results, however, no other measured monostatic results were compared with the dual-surface magnetic-field integral equation solution.

The next obvious step is to attempt to decrease the computer run time of the dual-surface magnetic-field integral equation solution when the angle of incidence is far from the z-axis of revolution. This can be accomplished by using a fast Fourier transform (FFT) to compute the phi integration for each mode. The FFT will save computer run time, for cases with the incident field off the z-axis, of about $2 \log_2 N/N$ times the current run time where N is approximately kr (see Eq. (63)) for the body of revolution program. The drawback to the FFT is the additional memory requirement. This could be overcome by using direct access files on disk as is discussed in Woodworth.¹⁴ By using direct access files, however, there is the added difficulty in computer programming, a greater CPU time requirement, and the possibility of a large increase in input/output time.

The addition of a geometry package allowing the user to input a variety of geometry types would greatly aid the use of the program. At the present time, the program accepts spheres, conespheres, cylinders, and cylindrical shaped frustums as input. The code was originally written to accept only a sphere as an input but the geometry input package of Reference 7 was modified to allow the other shapes to be used as input to the code. Other shapes would provide additional validation of the dual-surface magnetic-field integral equation solution as well as providing useful results to the users of the body of revolution program.

¹⁴Woodworth, M.B. (1988) *Large Matrix Solution Techniques Applied to an Electromagnetic Scattering Problem*, RADC-TR-88-268, Hanscom AFB, MA, ADA206917.

References

1. Murray, F.H. (1931) Conductors in an electromagnetic field, *Am. J. Math.*, **53**: 275-288.
2. Maue, A.W. (1949) On the formulation of a general scattering problem by means of an integral equation, *Zeitschrift fur Physik*, **126(7/9)**:601-618.
3. Yaghjian, A.D. (1981) Augmented electric and magnetic field integral equation, *Radio Science*, **16**:987-1001.
4. Tobin, A.R., Yaghjian, A.D. and Bell, M.M. (1987) Surface integral equations for multi-wavelength, arbitrarily shaped, perfectly conducting bodies, *Digest of the National Radio Science Meeting*, (URSI), Boulder CO.
5. Woodworth, M.B. and Yaghjian, A.D. (1989) Derivation, application and conjugate gradient solution of the dual-surface integral equations for three-dimensional, multi-wavelength perfect conductors, *PIERS-5: Applications of the Conjugate Gradient Method to Electromagnetic and Signal Analysis*, Sarkar, T.K. and Kong, J.A., eds., Elsevier; Also RADC Rep. TR-89-142, Hanscom AFB, MA, ADA229076.

6. Mautz, J.R. and Harrington, R.F. (1987) H-field, E-field, and combined-field solutions for bodies of revolution, *Arch. Electron. Ubertragungstech. (Electron. Commun.)*, **32** (4):157-164.
7. Wang, C.W. (1983) *Scattering From Rotationally Symmetric Conducting Body*, Ohio, State University ElectroScience Laboratory Tech. Rep. 714614-2, Columbus, Ohio.
8. Yaghjian, A.D. (1977) *Near Field Antenna Measurements on a Cylindrical Surface: A Source Scattering-Matrix Formulation*, NBS Technical Note 696.
9. DiBeneditto, J.P. (1984) *Bistatic Scattering From Conducting Calibration Spheres*, RADC-TR-84-93, Hanscom AFB, MA, ADA154173.
10. Stratton, J.A. (1941) *Electromagnetic Theory*, McGraw-Hill, New York.
11. Harrington, R.F. (1961) *Time-Harmonic Electromagnetic Fields*, McGraw-Hill, New York.
12. Waterman, P.C. (1965) Matrix formulation of electromagnetic scattering, *Proc. IEEE*, **53**:805-812.
13. Borgnis, F.E. and Papas, C.H. (1958) Electromagnetic waveguides and resonators, *Encyclopedia of Physics*, S. Flugge, ed., **16**, Springer-Verlag, Berlin.
14. Woodworth, M.B. (1988) *Large Matrix Solution Techniques Applied to an Electromagnetic Scattering Problem*, RADC-TR-88-268, Hanscom AFB, MA, ADA206917.

Appendix A

Integration Correction

The purpose of Appendix A is to obtain Eq. (47). For this integration let $t' - t = t'$ by letting $t = 0$. As shown in Figure A1, the integration of the Green's function for the ring containing the self patch involves the integral

$$I = \int_{\Delta t/2}^{\Delta t/2} \int_0^{2\pi} \frac{\sin^2(\phi'/2)}{R^{3/2}} d\phi' dt'. \quad (\text{A1})$$

This can be rewritten as

$$I = \int_0^{2\pi} d\phi' \int_{\Delta t/2}^{\Delta t/2} \frac{\sin^2 \phi'/2}{[(\rho - \rho')^2 + (z - z')^2 + 4\rho\rho' \sin^2(\phi'/2)]^{3/2}} dt' \quad (\text{A2})$$

by substituting for R from Eq. (26). For a fixed ϕ' the t' integration in Eq. (A2) can be written as

$$I_1 = \int_{\Delta t/2}^{\Delta t/2} \frac{1}{R^{3/2}} dt'. \quad (\text{A3})$$

For ϕ' small

$$R \approx \sqrt{R_c^2 + t'^2}, \quad (\text{A4})$$

where

$$R_c = \rho\phi' \quad (\text{A5})$$

and

$$t' = \sqrt{(\rho - \rho')^2 + (z - z')^2}. \quad (\text{A6})$$

Therefore

$$R \approx \sqrt{\rho^2\phi'^2 + t'^2}, \quad (\text{A7})$$

and so

$$I_1 = 2 \int_0^{\Delta t/2} \frac{1}{(\rho^2\phi'^2 + t'^2)^{3/2}} dt'. \quad (\text{A8})$$

For a small fixed ϕ' and integrating Eq. (A8), one obtains

$$I_1 = \frac{2}{\rho^2\phi'^2} \left[\frac{\Delta t/2}{\sqrt{(\Delta t/2)^2 + \rho^2\phi'^2}} \right]. \quad (\text{A9})$$

For a small fixed ϕ' and Δt approaching zero,

$$I_1 = \frac{\Delta t}{\rho^3\phi'^3}. \quad (\text{A10})$$

The same result will be obtained for a small fixed ϕ' from the following equation

$$I = \frac{\Delta t}{8\rho^3 \sin^3 \phi'/2}. \quad (\text{A11})$$

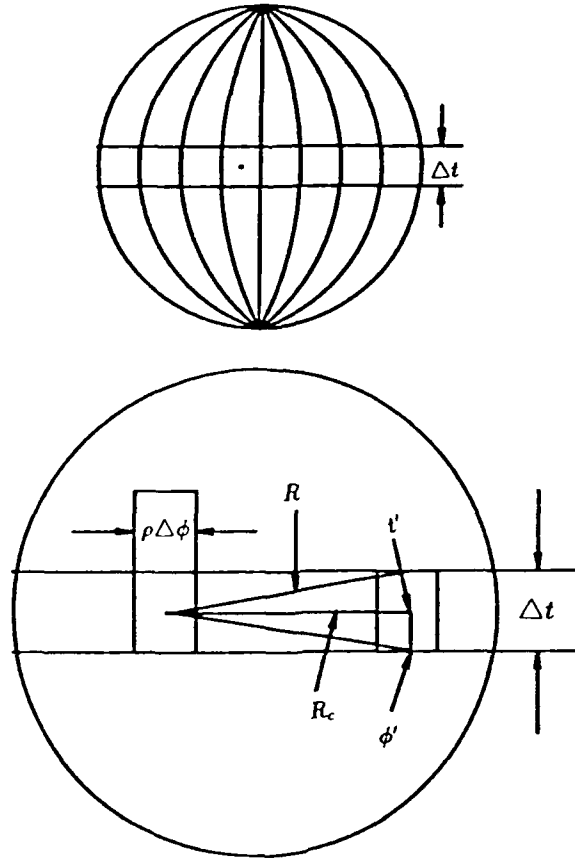


Figure A1: Phi Integration Correction for Self-Patch

This means that we are integrating

$$\Delta t \int_0^{2\pi} \frac{\sin^2(\phi'/2)}{8\rho^3 \sin^3(\phi'/2)} d\phi' \quad (\text{A12})$$

and we should be integrating

$$\Delta t \int_0^{2\pi} \frac{\sin^2(\phi'/2)}{\rho^2 \phi'^2 \sqrt{(\Delta t/2)^2 + \rho^2 \phi'^2}} d\phi'. \quad (\text{A13})$$

By substituting Eqs. (A9) and (A10) into Eq. (A12)

$$I = \Delta t \int_0^{2\pi} \frac{\sin^2(\phi'/2)}{R^2 R_c} d\phi'. \quad (\text{A14})$$

This $1/(R^2 R_a)$ in Eq. (A14) is the approximation for the most singular part of the Green's function in the phi integration that contains the self patch. For the remaining less singular part of the Green's function, R_c can be approximated by the mean distance

$$R_a = \sqrt{(\Delta t/2)^2/4 + (\rho\phi')^2}. \quad (\text{A15})$$

Combining this R_a approximation to the lesser singular part of the Green's function with $1/(R^2 R_c)$ in Eq. (A14), one obtains Eq. (47). The R_c approximation was originally derived for R so that the phi dependence could be integrated in very fine increments, but after running the program with phi integration segments much finer than Δt , it was determined that phi-segments approximately equal to Δt gave the greatest accuracy. It was also seen that the accuracy was better using the R_c correction than the correction of Reference 6.

**MISSION
OF
ROME LABORATORY**

Rome Laboratory plans and executes an interdisciplinary program in research, development, test, and technology transition in support of Air Force Command, Control, Communications and Intelligence (C³I) activities for all Air Force platforms. It also executes selected acquisition programs in several areas of expertise. Technical and engineering support within areas of competence is provided to ESD Program Offices (POs) and other ESD elements to perform effective acquisition of C³I systems. In addition, Rome Laboratory's technology supports other AFSC Product Divisions, the Air Force user community, and other DOD and non-DOD agencies. Rome Laboratory maintains technical competence and research programs in areas including, but not limited to, communications, command and control, battle management, intelligence information processing, computational sciences and software producibility, wide area surveillance/sensors, signal processing, solid state sciences, photonics, electromagnetic technology, superconductivity, and electronic reliability/maintainability and testability.